TECHNICAL REPORT

TEAM #12

ECLIFT
03/05/2025

III EDITION
VALÈNCIA

JULY 8 – 11 OF 2025

Contents

List of Figures

List of Symbols

$\|q\|_{bp}$	Battery capacity [mA h]
I_{max}	Maximum electric current [A]
T_{servo}	Torque of the servo [N m]
V	Velocity [$\mathrm{m\,s^{-1}}$]
c_f	Chord of control surface [m]
b_f	Length of control surface [m]
δ_f	Deflection of control surface [°]
θ_{servo}	Operational range of servo [°]
L/D	Lift-to-drag ratio [-]
C_L	Lift coefficient [-]
C_D	Drag coefficient [-]
C_M	Moment coefficient [-]
Re	Reynolds number [-]
MAC	Mean aerodynamic chord [m]
b_w	Wingspan [m]
S_w	Wing surface area [$\mathrm{m^2}$]
λ_w	Wing taper ratio [-]
$C_{M\alpha}$	Moment coefficient slope with angle of attack [-]
$C_{L\beta}$	Rolling moment coefficient with sideslip angle [-]
$C_{N\beta}$	Yawing moment coefficient with sideslip angle [-]
SM	Static margin [%]
x_{NP}	Neutral point position [m]
x_{CG}	Center of gravity position [m]
$C_{M\delta_e}$	Ruddervator control effectiveness [-]
$C_{L\delta_a}$	Aileron control effectiveness [-]
$C_{N\delta_a}$	Yaw induced by aileron [-]
$C_{L\delta_R}$	Roll induced by rudder [-]
ρ	Air density [$\mathrm{kg\,m^{-3}}$]
MPL	Maximum payload [kg]
$MTOW$	Maximum takeoff weight [kg]
OEW	Operational empty weight [kg]

1 Introduction

This report presents the design, analysis, manufacturing, and testing of a remote-controlled aircraft developed by ECLift for the 2025 XtraChallenge. The aircraft is engineered to maximize payload and gliding performance while complying with all structural, aerodynamic, and electronic constraints imposed by the competition.

Building on the experience and success of the previous year's design, this year's project emphasizes modularity, optimized composite structures, and system reliability. The report details the organizational methodology, electronic selection and evaluation, aerodynamic modeling, structural and manufacturing developments, and performance analysis.

Innovative aspects include the use of 3D printed plugs ans parting boards to make tooling coat molds, an integrated avionics bay for streamlined electronics management, and a removable water payload module. Manufacturing processes were developed to be both repeatable and cheap while maintaining a supreme surface finish and structural integrity.

The resulting aircraft, hence forth referred to as the ECTanker, demonstrates great structural efficiency, stable flight characteristics, and streamlined electronics integration. This new product offers a complete system solution that represents a significant improvement over last year's design. The ECTanker approaches near professional grade design and manufacturing thus posing itself as a highly capable platform for further avionic and propulsive enhancements.

1.1 The XtraChallenge

The XtraChallenge is a aeronautic engineering student's proving ground. It compels students to become the aircraft creator, balancing design, manufacturing, and testing all while being constrained temporally and financially. The competition takes place every year in Valencia, Spain, since 2023 and it is organized by the Xtra2 UPV team. In this competition, international collegiate aeronautics students' teams gather to present and fly original airplanes made by themselves in every aspect, following the restrictions of a series of regulations that change every year.

As the full replication of this years rules is unnecessary, only the most important are to be discussed, namely payload, circuit, and transportation. Water is the payload of choice, as to resemble the anticipation of hydrogen-transporting drones. The circuit follows the sequence: take-off, max rate of climb, max glide, pylons, landing. This sequence must remain for all rounds, however payload load is left to our discretion. The relative points associated with payload loading and circuit performance can be found in the official XtraChallenge rules. Lastly, the dis-assembled aircraft must fit in a $700x350X250mm^3$ box.

1.2 The École Centrale Lyon and ECLift

École Centrale Lyon is a French engineering university dating from 1857, located in Lyon. ECLift (read: "easy lift") is a group of students from the Master's in Aerospace Engineering program offered by this school. ECLift's activity began in October 2023, when thirteen members coming from seven different nations started working on the development on an aircraft for the XtraChallenge 2024. Since then, the team has doubled in size and depth. In July 2025, twelve members will travel to Valencia and participate in the contest while also showcasing their prototype in front of top-level competitors, academics, and companies.

2 Project Management

2.1 Team Structure

The ECLift team for the 2024–2025 season is organized into four main departments:

- **Aerodynamic Design and Simulation**
  Conducts all performance analysis related to airfoil and wing geometry, stability, and CFD

simulations. Above all, responsible for the aircraft's geometry choice.

- **Structures and Manufacturing**
  Designs, sizes, and validates the aircraft structure, and ensures manufacturability of all components. Fully concerned with the materialization of the airframe.

- **Propulsion and Onboard Electronics**
  Handles the powertrain analysis, component selection, integration of electronics, and layout of the flight system. Responsible for the design, implementation, and sustatinment of the aircraft's brain, control surfaces, and power plants.

- **Marketing**
  Engaged in the enhancement of online presence development, sponsor coordination, and group aesthetic. Defining the tone of the aircraft and project.

Each department is headed by a dedicated lead, appointed at the beginning of the 24-25 school year. With the member count being over twenty a simplified hierarchical chart is presented in Figure 1.

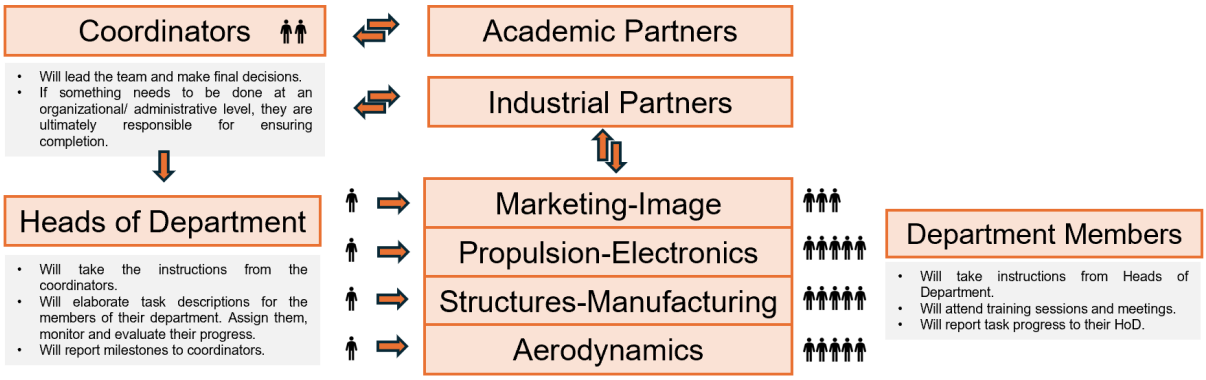

Figure 1: Organizational chart of the 2024–2025 ECLift team

2.2 Development Masterplan

In early August 2025 the decision was made by the head of departments to re-enter the Xtra-Challenge, subsequently plans were devised from general goals to specific tasks. Detailed Gantt charts and graphic timelines were developed for each sub team, for simplicity the Structures Team's graphic timeline, Figure 2, is given as an example.

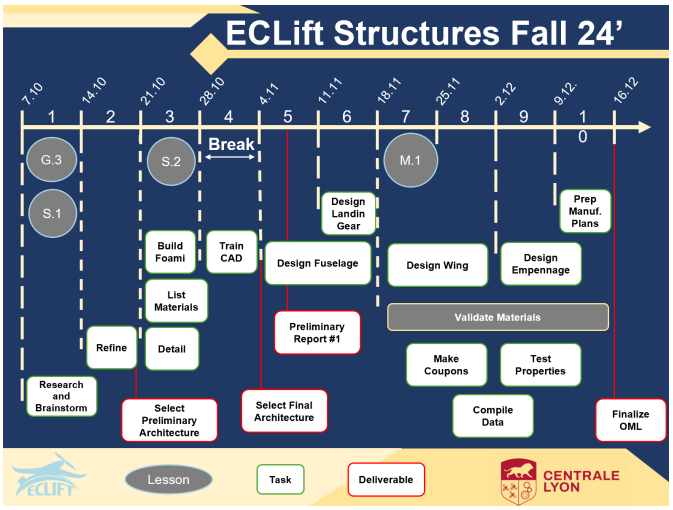

Figure 2: ECLift 24' structures graphic timeline

2.3 Sponsors

ECLift would not be possible without the support of our sponsors and collaborators:

Partner	Contribution
École Centrale de Lyon	Our premier French engineering institution providing academic, financial, and administrative support.
Laboratoire de Tribologie et Dynamique des Systèmes (LTDS)	A research laboratory offering guidance, access to testing facilities, and technical feedback.
Centrale Innovation	Facilitates industry-academia collaboration and helps promote innovation by supporting our technical initiatives.
Thales Group	A global leader in defense and avionics, contributing technical advice, sensors, and electronics to enhance system integration and autonomous capabilities.

Table 2: Key partners and their contributions to ECLift

2.4 Project Value

When discussing the project value, distinctions are made between the aircraft cost and project cost. This year a majority of funds was spent on composite components as all electronics and general consumables (i.e. wood, glue, ect.) were acquired the year prior. Therefore, the two largest components of project value arise from participation fees and construction materials. A total budget for the ECLift 24'-25' project is divided into categories as shown below:

Category	Cost [€]
Construction Materials	268.00
Consumables	219.35
Equipment	165.75
Registration Costs	1700.00
Total Project Value	**2353.10**

Table 3: Project cost breakdown for 2024–2025.

In terms of the aircraft cost, a much more detailed analysis is needed. A complete aircraft cost report is included in *Annex I: Budget Breakdown* where all relevant components of the aircraft and its construction is developed.

3 Electronics and Propulsion

This section describes all the electronic components installed on the aircraft which constitute both the flight control system and the propulsion system. In accordance with the competition's regulations, some of the component choices were limited to a given manufacturer's brand and model and some others were limited in terms of specifications. The strictly imposed components are the electric motor, Emax GT2820/06 985KV, and the propeller, with a possibility to choose from a selection pool of 4 propellers, either fixed or folding: APC 10x6E (fixed) / APC 10x6F (folding) or Aeronaut CamCarbon Light 10"x6"(fixed)/ Aeronaut CAM Z carbon 10x6 (folding). The components for which the limitations are imposed in terms of performance are the main battery, which should have 3 cells in series and not exceed 12.6V, and the ESC, which should allow for a constant current of at least 40A.

3.1 Propeller Selection

Considering the limitations of the competition, the highest thrust can only be obtained by figuring out which of the four available propellers offers the best performance when paired with the imposed electric motor. Finding the optimal pair is a critical aspect of the design process since the obtained thrust will influence the choices made in the plane's design and strategy. The optimization process was performed both theoretically, using MotoCalc software, and also through experimental testing using a dedicated static thrust measuring stand, which was in-house developed. The four propellers are both 10x6, lightweight propellers capable of producing high thrust.

Both the Aeronaut CAMcarbon Light propellers are made from carbon fiber, while the two APC 10x6 are made from a lightweight yet also resistant plastic. Despite the difference in materials, all propellers have similar weights below 30g. However, the folding propellers are slightly heavier than the fixed ones since they require an additional hub in order to be mounted on the engine, leading to an additional weight.

Better alligning with the design choice, a fixed propeller was selected to prioritize simplicity, structural rigidity, and consistent thrust delivery. While folding propellers reduce drag during gliding, the design emphasizes powered flight efficiency over unpowered glide performance. The fixed propeller offers reliable performance with fewer moving parts, aligning with the mission goals of minimizing mechanical complexity and maximizing propulsion reliability.

3.1.1 Theoretical Analysis

Considering the above mentioned, the theoretical analysis is conducted only for the two fixed propeller setups.

The MotoCalc software showed us that the difference between the two propellers is less than 10% in terms of thrust, but the highest value is obtained with the Aeronaut CamCarbon Light 10"x6" propeller and is about 1210g of thrust, as shown in Figure 3.

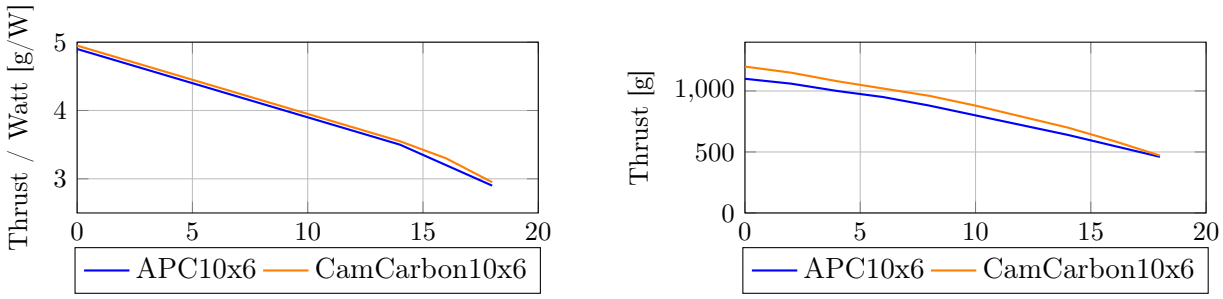

(a) Efficiency evolution with flight speed

(b) Thrust model for both propellers

Figure 3: Comparison of thrust and efficiency characteristics of APC10x6 and CamCarbon10x6 propellers.

By analyzing the efficiencies, we observe that the CAM Carbon 10x6 propeller is slightly more efficient on the entire flight airspeed range compared to the APC 10x6, but the difference is less than 3%. This is shown in Figure 3a , which presents the produced thrust per input Watt.

Because the predicted difference in thrust is less than 10%, and the differences in propeller efficiency and gram of thrust per input Watt are minimal, the selected type of propeller was the APC 10x6 propeller because of the reduced price and increased availability compared to the CAMcarbon 10x6 propeller.

3.1.2 Experimental Analysis

To validate the theoretical results, the electric motor, paired with the APC 10x6 propeller were mounted in the in-house developed static thrust testing stand. The motor run-up test was

performed up to 100% throttle and the values of the thrust were registered using a load cell connecting the engine mount to the bottom of the stand. At the maximum throttle setting, the experiment registered a value of 1079g of thrust, slightly lower than the estimated 1137g from the theoretical analysis.

3.2 Electronic Components

3.2.1 Electronic Speed Controller (ESC)

An effective speed controller was selected while complying with the regulation that it supports a constant current of at least 40A. SKYWALKER 50A V2 was selected as it delivers better performance when compared with other models of a similar price range.

3.2.2 Main Battery

The main battery was considered based on the flight circuit requirement and based on regulations as well. The initial step in accurately sizing the battery involves considering the following mission times:

- 10 seconds of take-off.
- 30 seconds of climb.
- 30 seconds of glide.
- 180 seconds of cruise (with a margin for missed checkpoints).
- 70 seconds for landing (accounting for a second attempt).

$$|q|_{bp} = c \cdot t \cdot I_{\max} = 1.2 \cdot \frac{320}{3600} \cdot 30000 = 3200\,\text{mAh}$$

Considering the total flight duration to be 320 seconds (5.5 minutes), the battery required to complete the flight needs a capacity of 3200 mAh.

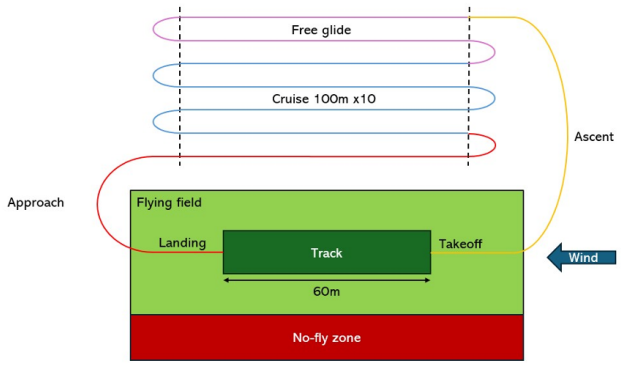

Figure 4: Flight Circuit

Based on the previous calculations for the minimum requirement of energy and also considered a safety factor, the ACCU LIPO SLS XTRON 3200mAh 3S 20C battery would be selected as it offers several advantages over other batteries. With a capacity of 3200mAh, it provides a balance between power and weight, ensuring longer flight times without significantly increasing the aircraft's weight. However due to our cost limitations, a cheaper generic soaring 3S battey is selected instead. The real capacity of the battery is usually lower than advertised, therefore we are still in the working range.

Compared to other brands, SLS (Stark Light Systems) batteries are known for their superior quality and reliability. They have lower internal resistance, resulting in less voltage drop under load. The voltage drop in the SLS XTRON 3200mAh 3S 20C is minimal, ensuring that our plane maintains power efficiency throughout the flight. This stability is critical in competitions where consistent performance can make a significant difference. Therefore, choosing the SLS XTRON battery over other options ensures better power management, longer flight times, and reliable performance, making it a superior choice for competitive flying. Again, despite these advantages we are forced to choose a cheaper battery due to budget constraints.

3.2.3 Servomotors

While choosing the servomotors, our main goal is to select components with a minimum weight and size, so that they can be integrated easily and seamlessly integrated in the wing structures, tail and empennage, while also being powerful enough to withstand and overcome the aerodynamic forces applied on the command surfaces in order to ensure that the plane can be controlled.

In order to estimate the torque applied on all the control surfaces, the following formula was used:

$$T_{servo}(V) = 3.06 \cdot 10^{-6} \cdot \frac{V^2 \cdot c_f^2 \cdot b_f \cdot \sin(\delta_f) \cdot \tan(\delta_f)}{\tan(\theta_{servo})}$$

Where: c_f is the chord of the control surface, in cm; b_f is the length of the control surface, in cm; V is the airspeed, in mph; δ_f is the deflection of the given surface, in deg; θ_{servo} is the operational range of the servo from the neutral point, in degrees.

For a variation of the velocity from $[0 \div 20]$ m/s, the variation of the torque is presented in Figure 5.

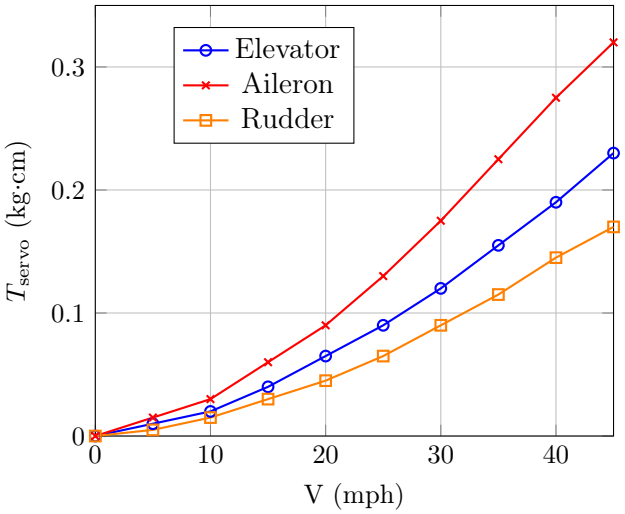

Figure 5: Torque analysis for different control surfaces across a range of airspeeds.

From this figure, we can observe that the most solicited control surfaces are the ailerons. Thus, the servomotors need to be strong enough to resist these aerodynamic forces.

For our targeted flight speed of around 15 m/s, we can observe that the maximum torque to which the servos need to resist is about 0.2 kg·cm; thus, we selected the EMAX ES3004 17grs/3.5kg·cm servomotor, which satisfies by far the strength criterion, while also being compact and relatively lightweight, making it very easy to integrate into both the wings and empennage. Another reason to select it was the fact that it is one of the cheapest full metal gear servos in the market. A feature that was considered a must for reliability reasons.

3.2.4 Auxiliary Battery

An Accu Lipo 2S 45C Black Lithium battery with a nominal capacity of 500mAh was chosen to power the flight controller, servos, and receiver. It is suitable since these components do not demand a significant amount of power, and it enables the isolation of the control circuit from power electronics for the safety reasons stated in the regulations.

3.2.5 Radio Transmitter and Receiver (TX-RX)

The Radio FS-i6 + Receiver FS-IA6 FLYSKY is selected as it is an excellent choice due to its reliable 2.4 GHz frequency operation, essential safety features like the programmable power cut-off lever, robust signal integrity with AFHDS 2A protocol, user-friendly interface, and affordability. These features ensure compliance with competition regulations, enhance safety, and provide a reliable and responsive control system, making it a superior option for competitive flying.

3.2.6 Voltage Regulator

Using the UBEC 4A Regulator for the auxiliary battery unit ensures a stable and efficient power supply for the plane's electronics. Its high current capacity and efficiency keeps the components safe. This regulator helps maintain consistent power and protects against electrical issues. A switch for ON/OFF the control circuit as well has been incorporated.

3.3 Circuit

The above-mentioned components are installed inside the body of the aircraft as presented in Figure 6.

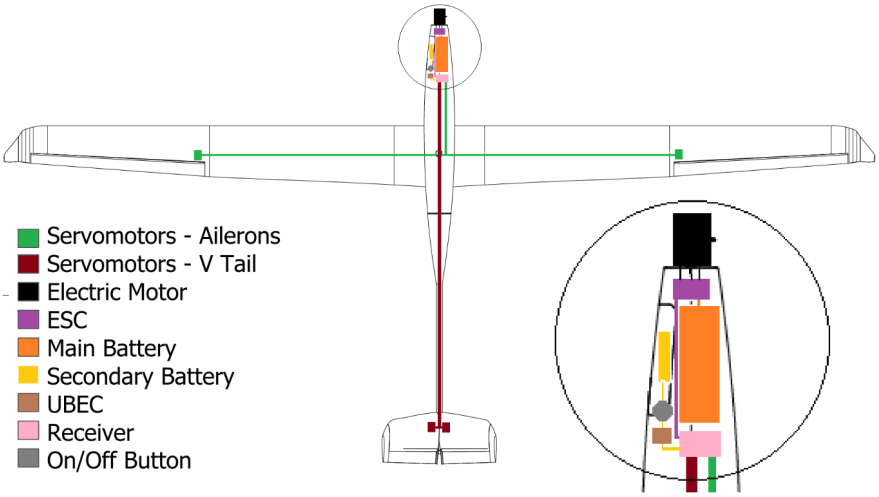

Figure 6: Electronic components layout

Inside each half-wing we can find one servomotors which actuate the ailerons. At the tail section we can find two other servomotors which control the ruddervators.

The electric motor is out-running, thus is installed outside the fuselage, in the nose section and is subjected to direct airflow for cooling. Also, in the nose section in the fuselage we can find stored all the other electronic components used to control the aircraft, the ESC, main and secondary batteries, the UBEC and the receiver.

In order to effectively turn on and off the airplane, in between the secondary battery and the UBEC, a two-positions button has been installed. Connections are ensured by lightweight cables which are neatly fixed to the inside of the airframe following the shortest possible path. Connectors grant easy disassembly of the aircraft without entanglement problems.

4 Aerodynamic Design

The aerodynamic configuration of the aircraft was developed through iterative analysis of the airfoil, wing, winglets, and tail surfaces to optimize performance under competition constraints. The airfoil was selected based on a favorable lift-to-drag ratio within the expected Reynolds number range, with validation through CFD simulations. Wing geometry—including span, chord distribution, and taper ratio—was refined via parametric studies to balance aerodynamic efficiency and structural feasibility. Winglets were introduced to reduce induced drag, and their effectiveness was quantified using CFD. The sizing and positioning of the ruddervator configuration were determined to ensure static and dynamic stability, while control surfaces were dimensioned to meet maneuverability requirements. Throughout the process, numerical analysis and graphical results guided the refinement of each aerodynamic component.

4.1 Airfoil Design

The aerodynamic performance of an aircraft is critically dependent on the design of its airfoil. Our approach commenced with a comprehensive analysis of various airfoil profiles which aid in maximizing glide while also operating at larger range of angle of attacks, evaluating each based on key aerodynamic metrics, such as the lift-to-drag ratio (L/D), lift coefficient (C_L), and moment coefficient (C_M). For the initial iteration, a Reynolds number (Re) of 2×10^5 was assumed. This process led to the identification of 9 promising airfoils. XFLR5 enabled a comprehensive assessment of these parameters under varying conditions, resulting in a reliable dataset for detailed comparison and analysis. The studied airfoils were in the range of [7,13]% thickness and [2,8]% camber in-order to achieve good glide ratio.

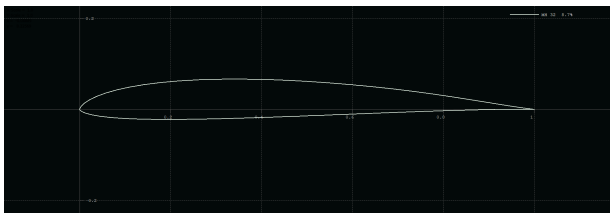

Figure 7: MH32 airfoil

The above process ensures that the final airfoil design meets the necessary performance criteria, paving the way for an optimized aerodynamic profile in our aircraft design and therefore, based on the XFLR analysis, MH32 airfoil was chosen. This choice was made based on its low C_{Dmin}, while having moderately good lift and finnese at small angles of attack as our primary objective was to have an airfoil with minimum drag to achieve good glide performance and lower angle of attacks.

In our assessment, we found that for the above airfoil, the lift coefficient is in the range [0.3, 1.2] for angle of attack ranging from 0 to 20. The drag coefficient is in the range [0.02, 0.09] contributing to lift-to-drag ratio spanning in the range [20, 75].

4.2 Wing Design

After selecting the airfoils, we advanced to the next stage of the preliminary design: proposing various wing configurations based on a conceptual sketch and verifying the model's static stability through three-dimensional analysis using XFLR5.

The wing dimensions were constrained by the fixed size of the transport box. Taking this into account, along with a parametric study of chord length, wingspan, and airfoil selection to determine the optimal sizing, we established that the allowable wingspan for our design fell between 2.5 meters and 3 meters. Additionally, the maximum allowable distance from the wing to the tail section was set at 0.8 meters.

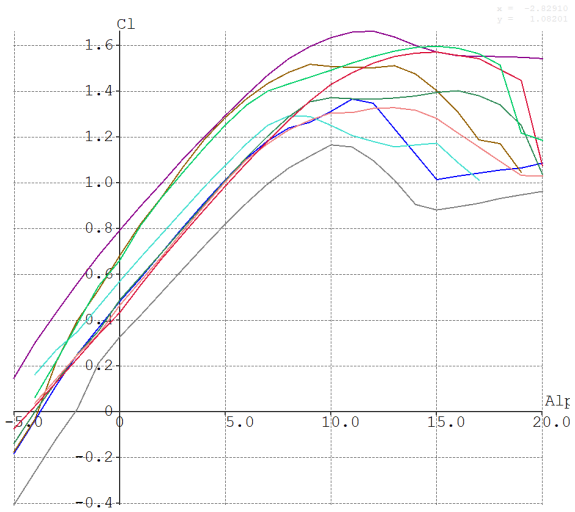

(a) (C_l) vs AOA (α)

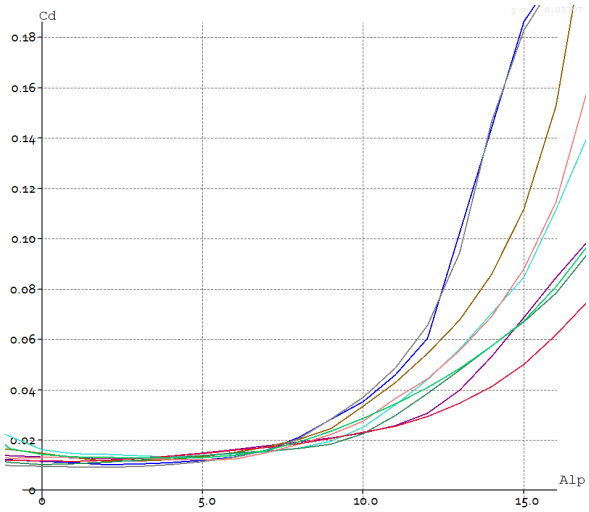

(b) (C_d) vs AOA (α)

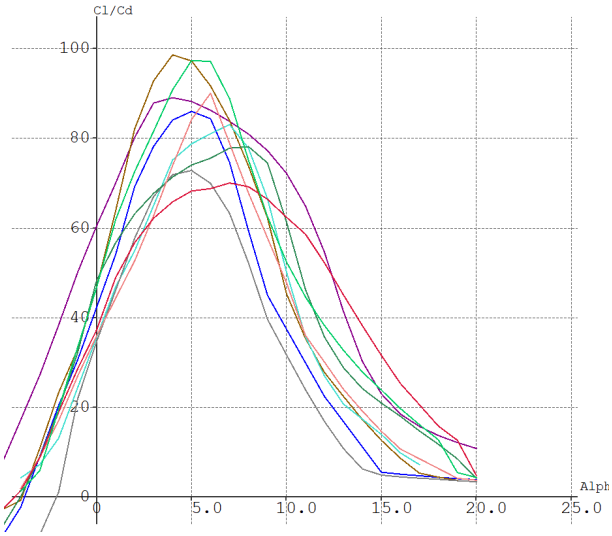

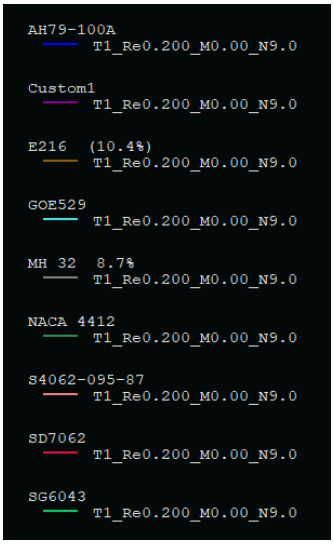

(c) Finnese (C_l/C_d) vs AOA (α)

Figure 8: Comparative airfoil performance evaluated using XFLR5 at $Re = 2 \times 10^5$.

The wing of the ECTanker — including chord length, spanwise offset, dihedral angle, twist angle, and airfoil type — was carefully selected to optimize performance. Based on these considerations, the final wingspan was determined to be 2.8 meters as to have an aerial advantage during the glide phase while also maintain an agile movement during the rest of the mission.

Parameter	**Symbol**	**Value**	**Unit**
Root chord	c_w	0.21	m
Wingspan	b_w	2.8	m
Wing surface	S_w	0.48	m^2
Taper Ratio	λ_w	0.40	–
Aspect Ratio	AR_w	16.17	–
Root-tip Sweep	$\Lambda_{c/4,w}$	0.28	°
Wing Dihedral	Γ_w	2	°
Wing Twist	θ_{tip}	1.5	°

Table 4: Wing geometry parameters

The chord length decreases from 0.21m at the root to 0.08m at the tip. The dihedral angle was gradually increased to a value of 2° and the twist angle was maintained uniformly at 1.5° at the tip section of the wing. The final design of the wing was adapted to facilitate easier manufacturing processes. These adjustments ensure that the aircraft can be produced efficiently without compromising on performance or safety standards.

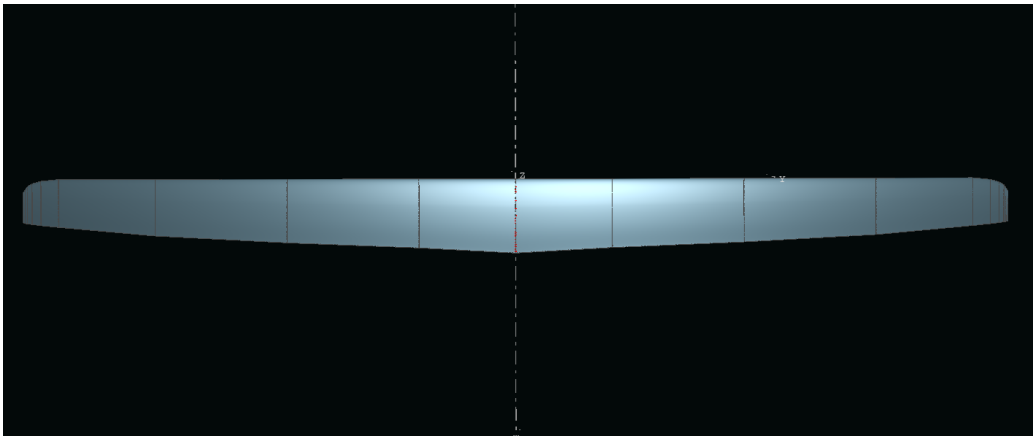

Figure 9: Final Wing Planform

4.3 Winglet Design

In our effort to maximize the aerodynamic efficiency of the aircraft, the design and selection of winglets became a key focus. We explored a range of winglet options to find the best fit for our wing configuration.

Using Autodesk Fusion 360, we created detailed models of different winglet types, including blended, sharklet, raked, and canted designs. Each one was carefully adapted to match the needs of our wing layout. To see how each design would perform, we ran CFD simulations in Ansys Fluent, mainly looking at their effects on drag reduction, lift improvement, and overall aerodynamic efficiency.

The CFD results gave us valuable insights into how each winglet affected performance. In the end, the sharklet stood out as the best choice for our wing. With its smooth, upward-swept shape, it proved highly effective at reducing drag by streamlining the airflow over the wingtips.

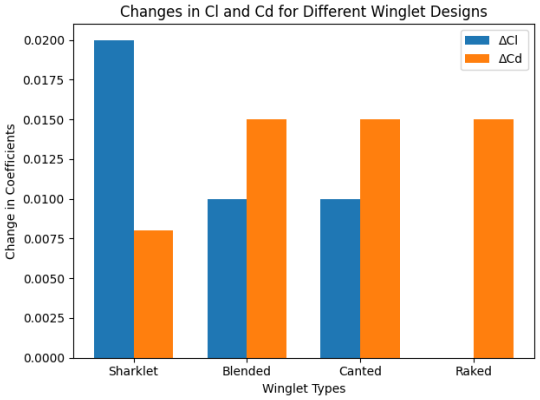

Figure 10: Comparative analysis of winglet types

The graph above shows the changes in lift coefficient (ΔC_L) and drag coefficient (ΔC_D) for various winglet designs, compared to a baseline configuration without a winglet. The baseline values are $C_L = 0.65$ and $C_D = 0.012$.

- The **Sharklet** winglet demonstrates the highest aerodynamic efficiency, achieving the greatest increase in lift ($\Delta C_L = 0.02$) while causing only a moderate rise in drag ($\Delta C_D = 0.008$). This indicates a significant improvement in overall aerodynamic performance.
- The **Blended** and **Canted** winglets provide moderate gains in lift ($\Delta C_L = 0.01$), but at the cost of a considerable increase in drag ($\Delta C_D = 0.015$), making them less efficient than the Sharklet.
- The **Raked** winglet shows no improvement in lift ($\Delta C_L = 0$) and results in a substantial increase in drag ($\Delta C_D = 0.015$), making it the least favorable option.

Thus, the Sharklet winglet is selected as the optimal choice due to its superior lift-to-drag ratio.

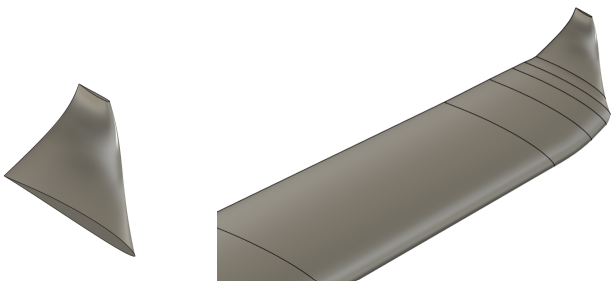

Figure 11: Final winglet design

4.4 Tail Design

The empennage, or tail assembly, of an aircraft is responsible for providing pitch and yaw stability and for housing the control surfaces. To meet the dual demands of climb under load and extended unpowered glide, we evaluated conventional straight tail, T-tail and V-tail and selected the V-tail for its clear advantages in drag reduction, weight savings and mixed-control authority. The following section details our V-tail geometry and control-mixing approach.

4.4.1 V Tail Design

The ECTanker sports a V-tail configuration, this was adopted to meet the competition's combined load-and-glide scoring. By merging the horizontal and vertical stabilizers into two surfaces set at a 45° dihedral, the V-tail reduces total wetted area and interference drag, directly improving the aircraft's lift-to-drag ratio during the unpowered glide. It also eliminates one fuselage intersection and one control surface, yielding a lighter empennage and simplified structure. The 45° split provides balanced pitch and yaw authority through mixed control deflection, ensuring equivalent stability margins in both axes. Key geometric parameters are summarized in Table 5.

Parameter	**Symbol**	**Value**	**Unit**
Mean aerodynamic chord	MAC	0.14	m
V-tail span	b_{vt}	0.60	m
V-tail surface area	S_{vt}	0.08	m^2
Taper ratio	λ_{vt}	0.44	–
Aspect ratio	AR_{vt}	4.48	–

Table 5: V-tail geometry parameters

(a) Top view (b) Isometric view

Figure 12: Final V-tail design

4.5 Aerodynamic Analysis

A CFD analysis (Finite Volume Method) conducted of the half model in Ansys Fluent at 0° angle of attack and a velocity of $10\frac{\text{m}}{\text{s}^2}$, the objective is to achieve a higher accuracy of calculations of the aerodynamic parameters and flow behaviour on the final plane design using 2 different CFD software with different methods. Table 6 showed the comparison of the C_L and C_D of the plane.

Software	C_L	C_D	L/D
Ansys Fluent	0.21	0.022	9.5
XFLR5	0.19	0.018	10.6

Table 6: Lift and drag comparison

Figure 13 shows the pressure coefficient (Cp) distribution obtained in ANSYS Fluent for the lowest-speed gliding condition. The distributed pressure over a large wing achieving acceptable lift in gliding phase.

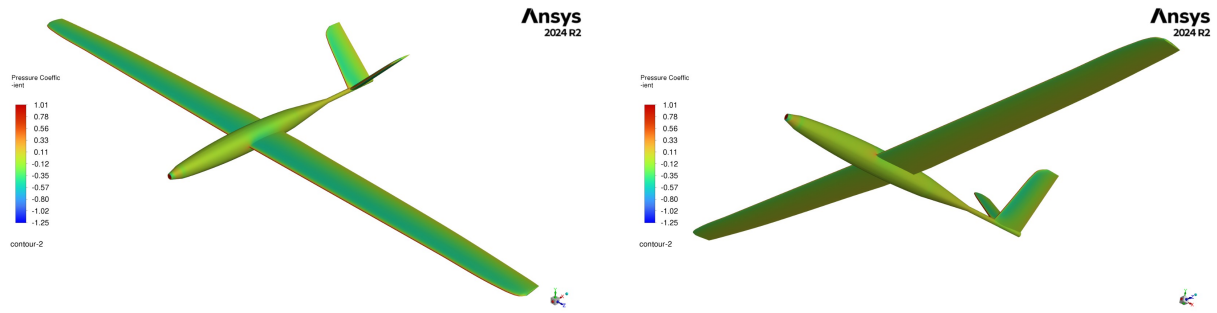

(a) Upper surface (b) Lower surface

Figure 13: Pressure coefficient (C_p) contours for the glider in low-speed glide

Figure 14a shows the Q-criterion iso-surface ($Q = 10\ \text{s}^{-2}$) with plane surface coloured by C_p, which highlights the wing-tip, tail-tip and minimal fuselage vortices responsible for most of the drag that generated from separation and induced one. Figure 14b shows the surface streamlines coloured by the skin friction coefficient, where the flow remains attached almost everywhere with only a small separation at the wing–fuselage junction (marked in red) that affects less than 1% of the wing area.

(a) Q-criterion iso-surface ($Q = 10\ \mathrm{s}^{-2}$) and C_p surface.

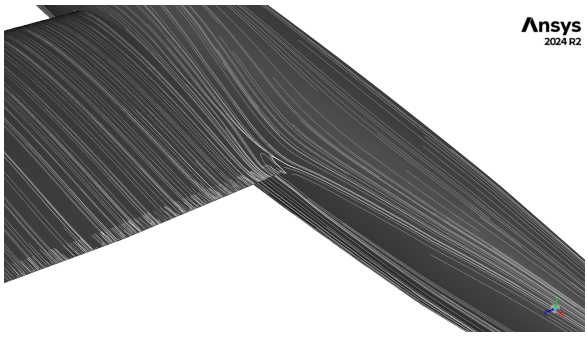

(b) Surface streamlines of skin-friction coefficient C_f.

Figure 14: Low speed glide flow visualisation.

5 Stability and Control

5.1 Stability Analysis

There are two different types of stability, static and dynamic stability. Statics is related to the generation of recuperative forces and moments, and dynamic stability indicates whether, under given reference conditions, the aircraft's response to any perturbations will reach a finite value.

In order to assume that an aircraft is statically stable, some requirements need to be fulfilled.

- The angle of attack at the null coefficient of momentum is not negative.
- The slope of the momentum coefficient with the angle of attack graph (C_{Ma}) has to be negative.
- The slope of the rolling momentum coefficient with the side slip angle (C_{Lb}) must be negative (lateral static stability criteria).
- The slope of the yawing momentum coefficient with the side slip angle (C_{Nb}) must to be positive (criteria of directional static stability).

Those values will be calculated in XFLR5 by a stability analysis without input conditions. In Table 7, the values obtained by the ECTanker are presented.

	$C_{Ma=0}$	C_{Ma}	C_{Lb}	C_{Nb}
ECTanker	0.044	-1.40825	-0.04728	0.04780

Table 7: Stability derivatives

The mass distribution of the ECTanker is essential to ensure a position of the center of gravity that would help the stability of the plane and reduce difficulties in maneuvering, even more so having a liquid load that could provoque sloshing. The total operational empty weight of the plane is 1.8 kg and is divided in the following elements:

Element	**Mass (kg)**
Fuselage	0.35
Tail Body	0.30
Landing gear	0.15
Whole Wing	0.80
V Tail	0.20

Table 8: Mass distribution

However, the stability analysis was performed with MTOW of 3.8kg, taking into account the maximum payload we believe the ECTanker is going to carry, of 2kg. The center of gravity of the ECTanker is positionned 0.039 m before the leading edge and 0.001 below it (loaded configuration).For addtional information, the empty fuselage but with the landing gear installed will have its center of gravity 0.056 m behind the leading edge of the plane, and 0.0006 below it.

It is extremely important that the center of gravity is situated before the neutral point. In the case of the ECTanker, the neutral point is situated at 8.2 cm of the leading edge, while the gravity center is at 3.9 cm of the leading edge. The static margin is calculated using the mean aerodynamic chord:

$$S.M. = \frac{|x_{NP} - x_{CG}|}{MAC} = \frac{|0.082 - 0.039|}{0.177} * 100 = 24\%$$

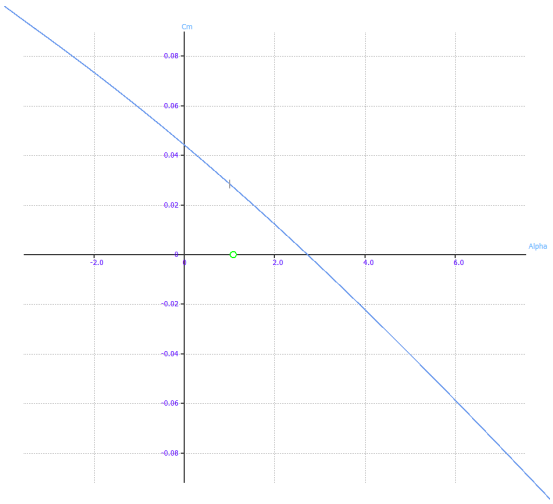

Figure 15: Longitudinal stability - C_m vs α

z

The dynamic stability is defined by the following graphics representing the stability eigenvalues or poles. These poles are considered stable when their real part is negative and they explain the answer of the aircraft when any input is introduced, and it can be calculated with XFLR5. It must be considered that some parts of the airplane, like the fuselage, were not introduced in the simulation and the real result may differ.

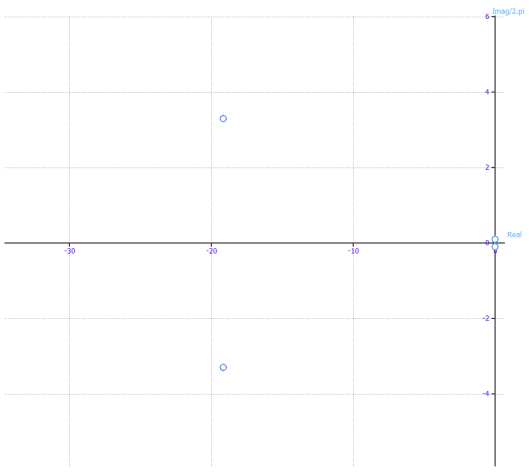

(a) Logitudinal Dynamic root locus

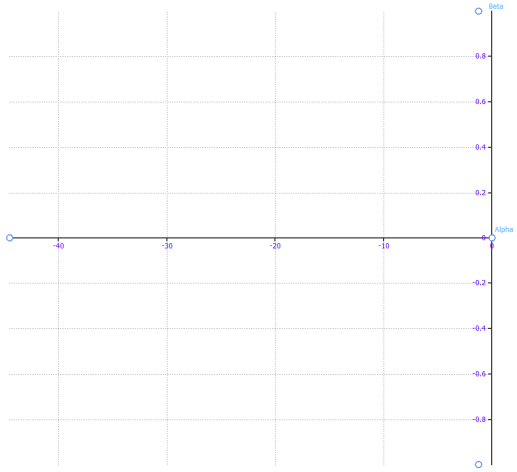

(b) Lateral Dynamic root locus

Figure 16: Dynamic stability plots

In Figure above, the poles of the final design with MTOW are presented. The first graph represents the longitudinal stability, which is in fact stable. In the lateral stability (second graph) it can be appreciated that one of the poles has minimal positive real value (around 0.04). This pole defines the spiral mode of the plane. However, this is such a small value that it was estimated that the pilot could easily counteract it.

Since a configuration with the maximum payload was presented here, in case of carrying a lower payload, the overall stability should improve, meaning the ECTanker will be stable for every possible configuration.
Finally, this analysis also provides the trim velocity at this weight, 66.6 km/h.

5.2 Control Surfaces

With a wingspan of 2.8m and a V-tail configuration, ECTanker is equipped with ailerons on the main wing and ruddervators on the tail, which serves the combined function of conventional horizontal and vertical stabilizer. The dimensioning of the control surfaces is chosed based on certain aerodynamic stability criteria that needs to be fulfilled ensuring the chosen dimensions are enough for the aircraft performance.

- The slope of the pitching moment coefficient with elevator deflection ($C_{M\delta_e}$) should be negative, indicating elevator effectiveness and its role in controlling pitch and climb.
- The slope of the rolling moment coefficient with aileron deflection ($C_{L\delta_a}$) should be positive, reflecting the ailerons' effectiveness in roll control.
- The slope of the yawing moment coefficient with aileron deflection ($C_{N\delta_a}$) should be close to zero, representing minimal adverse yaw due to aileron input.

Based on the above criteria, the following dimensions were chosen.

- The ailerons will cover 43.7% of the wingspan and 25% of the chord.
- The ruddervators will extend across the full span of the V-tail and cover 25% of the chord.

Since ailerons are positioned near the wing tips and are responsible for roll control, a delibrate gap of 5 cm is maintained between aileron and wingtips. This is done to minimize the risk of tip stall. This will allow the wingtip to remain unstalled longer. A gap is also maintained between aileron and flaps to ensure easier and unrestricted movement of both of them. This prevents mechanical interference during deflection and ensures smooth independent operation.

	$\mathbf{C_{M\delta e}}$	$\mathbf{C_{L\delta a}}$	$\mathbf{C_{N\delta a}}$	$\mathbf{C_{L\delta R}}$	$\mathbf{C_{N\delta R}}$
Definition	Elevator efficiency	Aileron efficiency	Induced yaw	Induced roll	Rudder efficiency
Criteria	< 0	> 0	≈ 0	> 0	< 0
ECTanker	-1.2061	+0.4194	+0.0004	+0.0001	-0.0000

Table 9: Control derivatives

6 Structural Design

With the addition of composite materials in this years competition, large complexities arose with respect to the structural design. Furthermore, with a budget of €400 being imposed there is increased analysis needed in the choice of materials, manufacturing processes, and overall

structural members. On the other hand, the addition of composites allowed for the development of streamlined bodies and efficient structural design.

Thanks to the teams refined background in composite design and manufacturing many questions were immediately clear. Firstly, the internal structures may be greatly reduced when a composite skin is introduced. Secondly, through a back of the envelope calculation, it was seen that staying in the budget would not be possible for a fully composite aircraft due to our desire to utilize high quality tooling coat molds.

In the world of composite manufacturing there are many ways to create a load bearing skin, however for the sake of smooth surfaces, replaceable parts, and close alignment, a top-bottom tooling coat and fiberglass mold methodology is effective. Despite their advantages, tooling coat molds can be costly to make and require long development times to produce a quality product. More details on mold manufacturing techniques will be given in section 7.

The structural design process started with the typical research and bench marking of relative sized planes. From there, design refinement and detailing took place followed by material research and CAD design. The resulting aircraft features a composite blended wing fuselage, composite skin inboard wings, wooden outboard wings with composite spars, a carbon boom tail body connection and wooden v-tails with composite spars. The assembled aircraft is shown in Figure 17 with all 5 major bodies highlighted.

The structural design was carried out with careful attention paid to the rules (namely cost), desire to decrease the loading time, and to increase payload capacity. The following section details the fuselage and wing designs with wing loading analysis and flight envelope development.

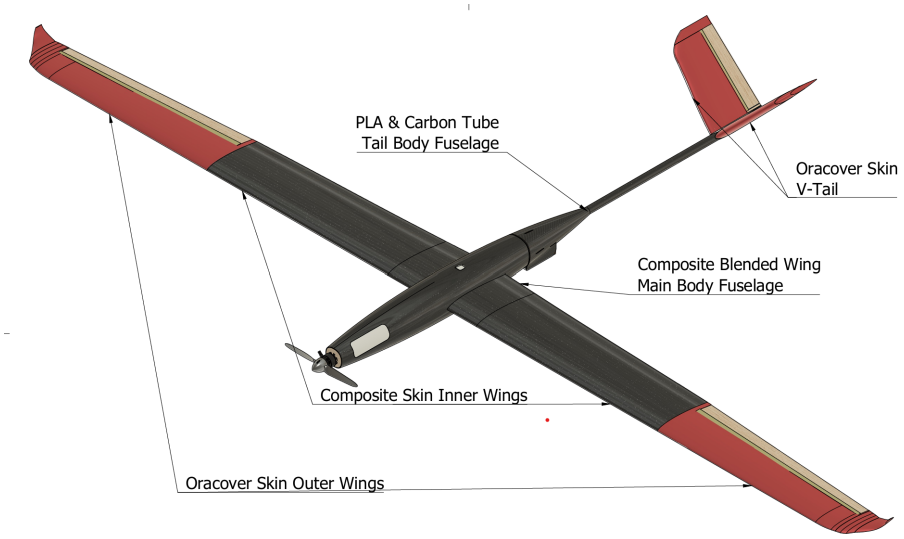

Figure 17: An isometric view of the assembled ECTanker.

6.1 Fuselage Design

To conform to the imposed box dimensions, the fuselage of the ECTanker has been separated into two sections, a Main Body and a Tail Body. The following two subsections discuss the design and components of the fuselage sections. For the main body, the following is discussed: avionics bay, water tank and loading method, wing–fuselage connection, landing gear, and hatches. The latter touches on the tail body and its v-tail to tail boom connection, main body to tail body connection, servo connections, telemetry box attachment, and landing gear.

6.1.1 Main Body

The main fuselage section of the ECTanker houses all the mission critical components of the aircraft, save for the control surfaces and telemetry box. In order to increase its strength while decreasing drag a composite skin was chosen. The section features a blended wing body to improve

structural efficiency for the wing-box loading while meeting aerodynamic desires. Furthermore, the back end section is left open to allow for easy payload access and tail body connection.

This body features a composite skin comprising 1 layer of 210g Plain Weave 3K Carbon Fiber and 1 layer of 100g 2x2 plain weave Fiberglass, material coupon tests were conducted before hand to ensure adequate strength. Further justifications for composite skin composition choices are given in section 7.

Beyond the load bearing skin, four formers and one stringer are added to allow for easy payload loading and secure transit. Since these internals are non-structural they are made of lightweight 3mm plywood. Additionally, four ribs, the closing former, and one firewall are present in 5mm plywood due to their structural nature. All structures are bonded to the skin via a epoxy, glass sphere, and milled carbon fiber mixture. Figure 18 presents an exploded view of the main body.

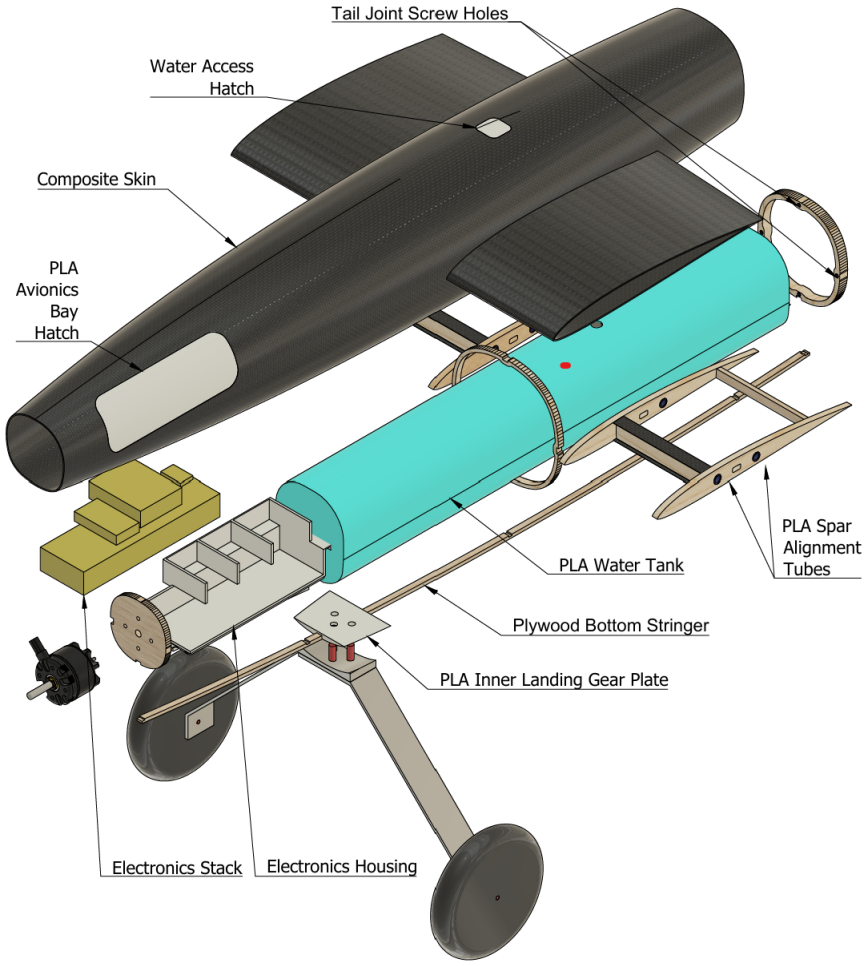

Figure 18: An exploded view of the main body fuselage.

Various sub-assemblies latch onto the main skin, including the avionics bay, landing gear, wing–fuselage joints, payload storage, and hatch access.

Starting at the nose of the airplane, the body is sized in such a way that we do not need to remove the motor for loading into the box. The motor holes are lasered into the firewall to ensure accuracy of the thrust line. Learning from our previous aircraft, almost a quarter of skin is removed from nose section to make way for a large avionics hatch. The weight of the 3D printed hatch is kept to a minimum thanks to special lightweight PLA. Also, a 3D printed shelf is present to ease cable management and straps are installed to securely load the powerplant.

Past the nose, the water tank is housed along the full length of the body. The CG of the water is placed intentionally to minimize the effects of payload on the CG. The water is contained

with 3D printed tank which is printed as a thin shell and reinforced with an epoxy paste. The shape of the tank is formed to sit in junction with the lower skin and stringer, and subsequently friction fit. Different sized tanks are made to allow for variable weight loading while maintaining proper CG positioning and non sloshing tanks.

The liquid loading is conducted through a small hatch at the top of the skin. There is a hole present in the top of the tank, which is sealed by a rubber gasket, whose size matches that of a typical funnel. Therefore, the fast loading will be carried out by quickly opening the hatch and the gasket followed by a funneling of water. In this way, the tank never needs to be removed for loading.

Below the water tank is the load path for the landing gear where a 3D printed reinforcement sits. It is added to the inside of the lower skin to provide a proper attachment points for screws. The print also has the bottom stringer profile impressed to allow for precision placement. The aluminum wheel assembly itself is off the shelf.

The joint that allows for the wing connection sits in the wing sections of the fuselage main body. It consists of simple 2x5mm plywood ribs that are post-bonded into the skin. The holes of the connector are fitted with PLA tubes to ensure proper alignment and easier assembly. The connector itself is are two 8mm diameter carbon tubes.

Finally, the rear of the main body is dedicated to the tail body attachment. A reinforced former with pre-drilled holes allows for the tail body to be easily and securely connected. More will be discussed in the following section.

Overall, the integrity of the main body fuselage is fortified by its composite skin. This thin and light structure will easily absorb the forces of flight, however in the tragic happening of an accident it will be relatively difficult to fix.

6.1.2 Tail Body

The tail body fuselage has many less tasks than its predecessor. Most importantly, it must have high torsional and bending rigidity to allow for smooth empennage operations. Furthermore it must reliably connect the v-tail to the tail boom. As adding more weight to the rear section was undesirable aerodynamically, an 20mm diameter carbon boom was selected to connect the tail to the body.

To reduce the drag penalty incurred by the sudden jump in geometry, a 3D printed cone-shaped diameter reducer is added. Combined with the 3D print is the telemetry box mount, fuselage connection screw holes, and wire storage. Figure 19 depicts the tail body.

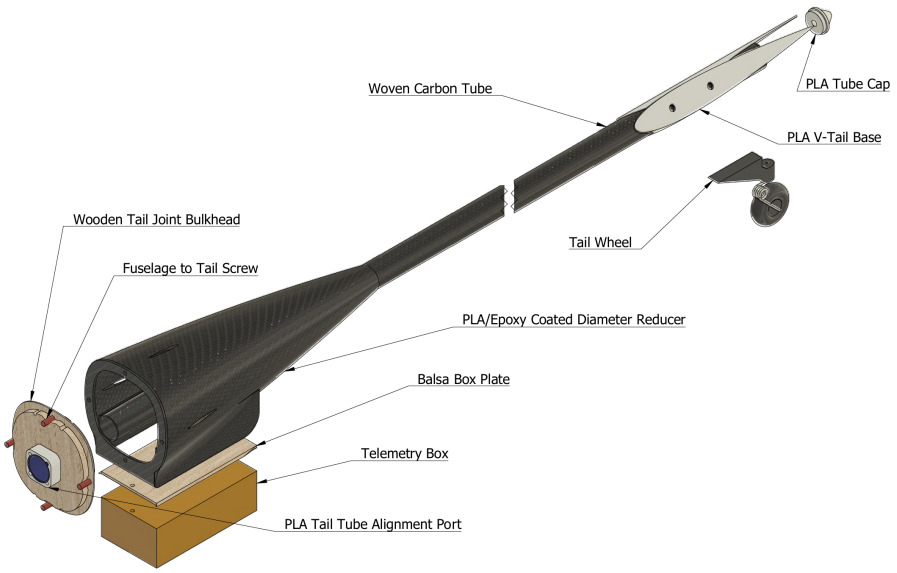

Figure 19: An exploded view of the tail body.

A sort of wooden door is added to the base of the diameter reduced to fit like a key into the rear of the open main body. The apparatus was designed to transfer the torque and bending of the tube, through the connection, into the main body. The leading bulkhead has screwed holes that match up with the end former of the main body.

Wiring for the ruddervator servos are channeled through the tube. One gear is connected in pair with the rear landing gear to increase taxi handling. The tail landing gear is a simple off-the-shelf component that is strung together using fishline. It is a great, low-weight, effective component.

To connect the v-tail to the tube, a 3D printed component is designed that wraps around the tube. It has four holes in which are slight offset to allow spar access. Various iterations of the component were seen, and a lightweight PLA was found to be reliable while remaining cheap and fast to produce for its small size. Additionally, a 3D printed tube cap is added to close out the tube while allowing for easy wiring of servo cables.

6.2 Wing Design

Like the fuselage, the wing is split into two sections to fit in the enforced box size. Inner and outer wing sections are designed to work in concert to create the 2.8 m wingspan. As the inboard wings see greater loads, a composite skin was desireable in this section. However, for the outboard sections, cost compelled the use of wooden architecture and composite reinforcments.

The following two subsections discuss the design and components of the wing sections. For the inner wing, key topics of composite skin, wing to wing and wing to fuselage joints, and internal reinforcments are discussed. For the outer wings, key topics of wooden architecture, composite reinforcment, winglet connection, servo instillation and control surface reinforcement are discussed.

6.2.1 Inner Wing

The inner wing features a stunning composite skin that carries a majority of the loading, transfering it through four 5mm carbon spar-tube connections located at its root and tip sides. The root set connects into the fuselage ribs while the tip set connects the outboard wing to the inner. Ribs and shear webs are present to reinforce the structural rigidity and allow the thin carbon shell stiffness. Furthermore, a unidirectional carbon tape is applied to provide adequate loading path for bending. In Figure 20, an exploded view of the inboard wing is shown.

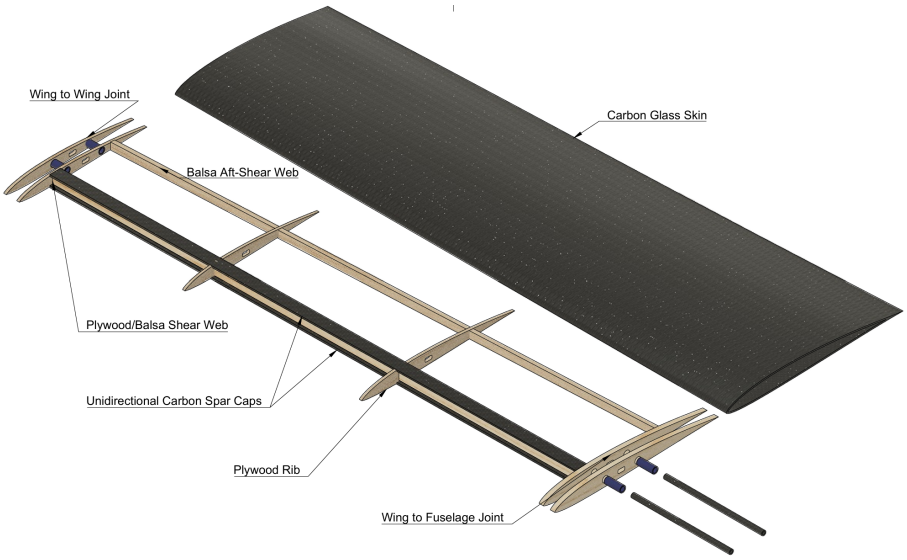

Figure 20: An exploded view of the inboard wing.

The joint sections of the wing are comprised of two ribs, 3D printed alignment tubes and a low-density epoxy paste in between the two ribs. The paste is added to prevent buckling and compression effects around the joint while adding relativly no cost and weight. More details of the paste is given in the manufacturing section.

All ribs have center holes for servo wiring. Non-joint ribs are split in two to allow for a constant span spar. A balsa aft shear web is added to ensure a non-compressible structure at the trailing edge of the secion.

Most important to this section is the composite skin, and indeed it is the most complex to discuss. Our R&D led us to choose a simple carbon-glass layup for the skin, however glass-balsa-glass skins were tested as well. With the carbon skin we achive a lighter body at the drawback of greater cost, increased internal reinforcments, and complexity with respect to fabrication.

For the competiton, our performance wings will be of the carbon composition, however we will have backup pairs of glass-blasa in the event of emergency.

6.2.2 Outer Wing

The outboard wing section is much more complex then its predecessor. Firstly, a plywood skeleton is present with 8 ribs, 6 doublers, two main spars, and a aft shear web. To reinforce the skeleton unidirectional carbon tape is used for spar caps and the leading edge. The addition of the carbon tape allows for easier application of the oracover plastic skin. In Figure 20, an exploded view of the outboard wing is shown.

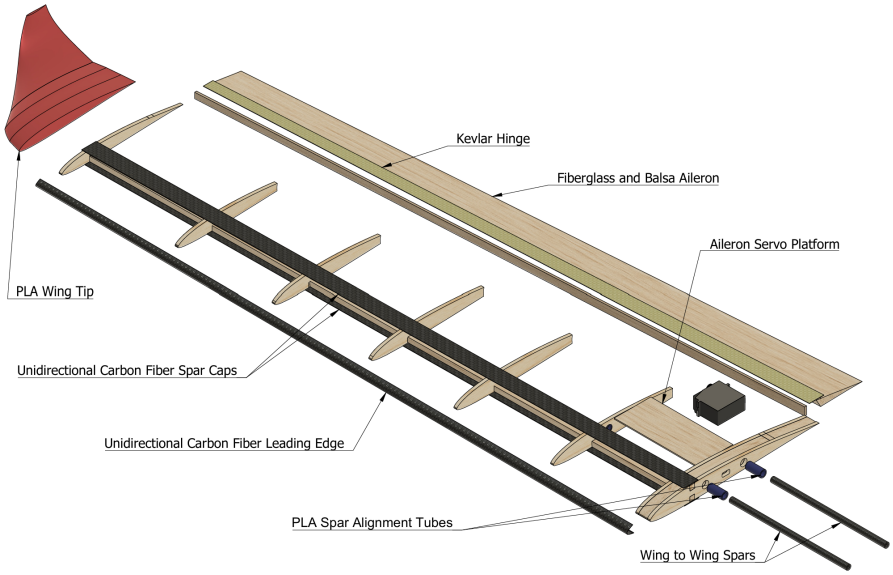

Figure 21: An exploded view of the outboard wing.

Of great interest in this section is the control surface and its design for reliability. Two main factors constained our airlerons actuation. Firstly, the super thin chord of the outboard wing demanded that the servo be placed at the wing root as to not purturde past the outer skin line. Therefore, with the servo being not at midspan, the fear of uneven torque was immediatly recongized which could lead to undereffective control authority. To remedy this, the balsa airleron is covered in a thin fiberglass layer to efficivly create a rigid sandwhich. Futhermore, a kevlar strip is used to permenatly connect the control surface to the fixed wing body. Futher details of this is given in the manufacturing section.

To ensure compliance to the aerodynamic design, a 3D printed wing tip was developed. This allows for the sharp geometry of the part to be fully realized. A thin PLA peice is coated with the lightweight epoxy paste and sanded to a super smooth finish. The wing tips are joined to the body via a high strength adhessive.

6.3 Empennage Design

The empennage is completely synonymous with the outboard wing section. The only major change is the use of a wooden leading edge, this can be seen in Figure 22. The wooden leading edge is selected due to the desire to simplify the manufacturing process.

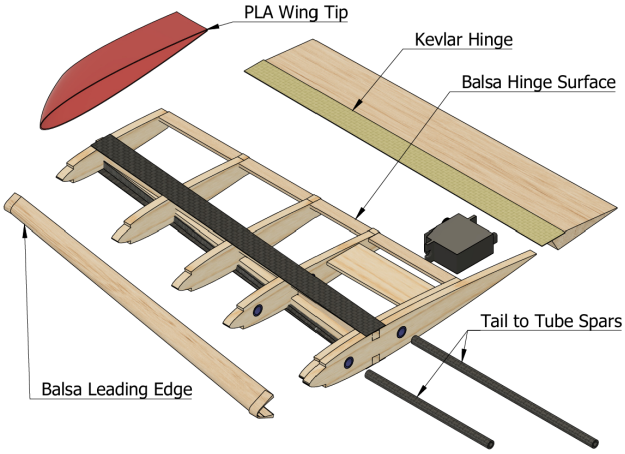

Figure 22: Exploded View of a V-Tail half

6.4 Static Bending Analysis

To evaluate the structural stiffness of the composite wing, a static bending test was conducted. The inner and outer wing panels were first joined using the internal spar tube and tape. With the wing secured horizontally at the root section, incremental point loads ranging from 1 to 5 kg were applied symmetrically at the wing tip, in steps of 0.5 kg. At each load step, the maximum vertical deflection at the mid-span was measured using a ruler.

Figure 23 shows the load-deflection relationship observed during the test. The resulting curve confirms that the wing behaves linearly in the elastic range up to 5 kg per tip, with no signs of permanent deformation or audible delamination.

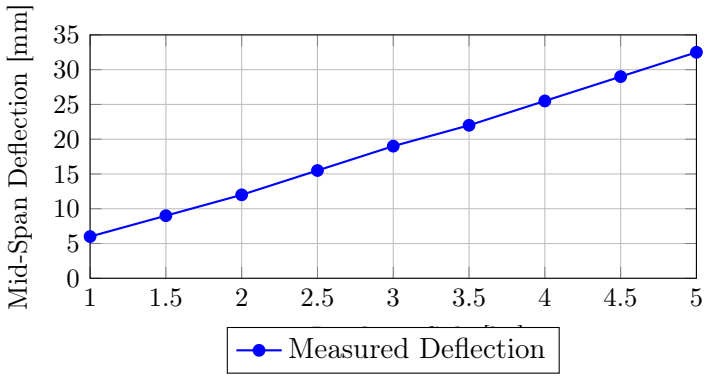

Figure 23: Mid-span wing deflection vs. tip load for static bending test

6.5 Flight Envelope

To assess the structural limits of the aircraft under varying aerodynamic loads, a MATLAB program was used to generate the V–n diagram shown in Figure 24. The tool calculates the maneuvering and gust envelopes based on key input parameters related to flight dynamics and aircraft geometry.

The following input values were provided to the MATLAB script to generate the flight envelope: a total mass of 3.8 kg, a wing area of 0.48 m^2, and a maximum positive load factor of 3.5. The maximum lift coefficient ($C_{L_{max}}$) was set to 1.08, and the cruising speed was defined as 15 m/s. The aircraft was categorized as a "Normal" type, reflecting standard RC-class assumptions used for maneuvering limits and dive speed calculations.

Based on these parameters, the program calculated a stall speed of 9.82 m/s, a corner (maneuver) velocity of 18.37 m/s, and a dive speed limit of 19.5 m/s. The maximum positive load factor was capped at $n = 3.5$, which is a conservative choice for composite RC aircraft operating in moderate flight profiles.

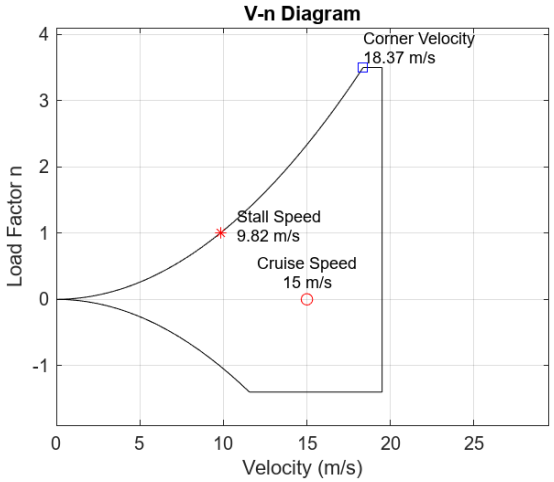

Figure 24: V–n diagram generated in MATLAB showing stall speed, corner velocity, and dive speed limit.

7 Manufacturing

This section will detail methods used in the manufacturing of the ECTanker. Located at École Centrale, the FabLab facilities were exclusively used; 3D printing, laser cutting, soldering, and many other processes were carried out in the facility. With the development of composite structures come many avenues of work that must be addressed for a quality final product. Therefore, special attention was paid to defining and detailing each step needed to create the composite structures. For the composite bodies, the creation process was divided into three main phases: mold creation, skin production, and body assembly. Each phase was conducted to deliver a high-performance structure and surface finish.

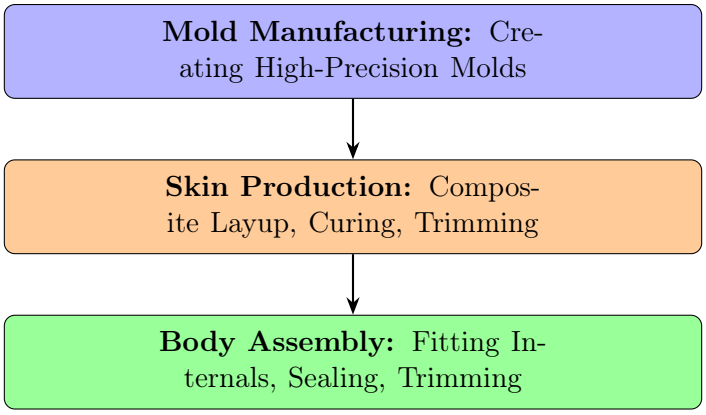

The primary materials used in the creation of the ECTanker were wood (balsa, ply), lightweight PLA, adhesives (CA, epoxy-glass bubbles paste), carbon fiber, fiberglass, and Kevlar. The most

used non-composite material was 2.5mm plywood. This strong and tough wood constitutes the backbone of the non-composite skin sections. In the composite sections, carbon fiber was the primary fiber of choice.

The following sections serve to highlight the key processes taken in the creation of the ECTanker bodies. First, the main steps in the composite process are detailed, followed by the Oracover skin bodies creation and tail body assembly. It is the goal of this section to provide the reader with a holistic review of the steps needed to create the ECTanker.

7.1 Phase I: Mold Creation

As was previously discussed, a top-bottom tooling coat mold was desirable and therefore demanded that plugs and parting boards be developed for each needed body. Plugs serve as positive models of the aircraft components and therefore represent the exact external shape of the final body. Parting boards, by contrast, define the split between the mold halves and serve as a boundary surface when applying the tooling coat.

Since we aimed for top-bottom mold configurations, each component required a plug and corresponding top and bottom parting boards. For our design, this resulted in two wing plugs, one fuselage plug, four wing parting boards, and two fuselage parting boards. While traditional plugs and parting boards are made of high-density foams, our lack of resources led us to pursue 3D-printed bodies instead.

Once the desired solid body model was complete, .STL files were generated and sliced to begin the process of printing the "pre-molds." Using Prusa MK4S printers, we created both plugs and parting boards in segments that were carefully joined with CA glue. From there, the surface refinement began: sanding and priming cycles were repeated 6–8 times to achieve the smoothest surface possible. Once the plug fit perfectly in its mold, and its surface was ultra-smooth, clay was applied around the plug to create a seal between it and the parting board. This seal ensured that the following tooling coat would not leak under the part. Then a PVA release agent was applied in two layers to allow the mold to be separated cleanly after curing.

Once prepped, one coat of a tooling coat epoxy was applied with bubble removal done actively to preserve surface clarity. It should be noted that two coats of tooling epoxy would have been desirable for multiple reasons; however, our strict budget demanded the bare minimum be used of this expensive epoxy. Once the tooling epoxy had reached its gel state, we laminated multiple layers of thick fiberglass and epoxy over the tooling coat to create a solid mold shell. After curing, each mold was trimmed and imperfections were addressed using a wet sanding process and epoxy-glass filler. When one mold half was completed, its opposite was made using the original plug. The end of the process resulted in professional-grade molds ready for skin production. Figure 25 gives an example of the mold-making process.

(a) Tooling coat applied to the plug and parting board

(b) Fiberglass fabric laminated over the mold and tooling coat

Figure 25: Steps in the mold preparation process for the upper fuselage section

7.2 Phase II: Skin Production

With molds complete, the next task was to produce the aircraft's composite skin. Each mold was cleaned of any debris, waxed four to five times, and coated with release agent. The layup process began with carefully measured and cut layers of fibers and core materials all staged in an organized workflow. A epoxy paste mixture is squeezed into tight angles to ensure no voids. Each layer was saturated with epoxy resin and applied to the mold quickly. Unidirectional carbon fibers are applied on the final layer to ensure correct orientation.

Once the layup was complete, we transitioned to vacuum bagging. This involved laying down perforated film, breather cloth, and then sealing the mold in a vacuum bag using sealant tape and a vacuum hose. The layup was left to cure under vacuum for 18-24 hours depending on the hardener choice. When fully cured, the composite skins were demolded, washed, and trimmed to a consistent flange size using a diamond disk, preparing them the bonding process. Our first skin produced was a glass-balsa-glass composition as can be seen in Figure 26.

Figure 26: Post-layup of the balsa-fiberglass wing

7.3 Phase III: Body Assembly

Bringing the aircraft body together started with fitting all internal wooden structures such as ribs, stringers, and formers. These were laser cut and had to fit into one skin half, which remained taped in the mold to maintain shape. Careful sanding ensured each internal matched its exact location and fully contacting the skin surfaces is paramount to the structural reliability.

With everything aligned, we mixed a custom adhesive known as "Kitchen Sink"—a blend of epoxy, carbon fiber shreds, and glass microspheres. This blend is extremely strong, light, sandable, and most importantly, cheap. A thin bead of adhesive is laid in the bottom skin, internals placed, and fillets made on the corresponding edges. The bottom is allowed to cure, then a final skin fit is made to ensure proper internal alignment. At this stage, wires are run and taped down for servos in the tail and wing.

Lines of adhesive were then laid across all points of contact. The process required precision to ensure all contact surfaces were covered without applying excess weight. Once all desired surfaces were covered in adhesive, the top skin was placed and weighted evenly across the structure, then left to cure for 24 hours.

After opening the mold, the mold lines were trimmed, edges sanded, hatches/holes were cut,

and tips trimmed. Finally, any exposed seams were reinforced with epoxy-impregnated strips of fiberglass. Additionally, any imperfections were filled with a lightweight epoxy glass-spheres mixture and sanded. The root of the inner wing, made of balsa and fiberglass, is shown in Figure 27b. It is worth noting that this image was taken immediately after the body was released and therefore has yet to be sanded to a flat profile.

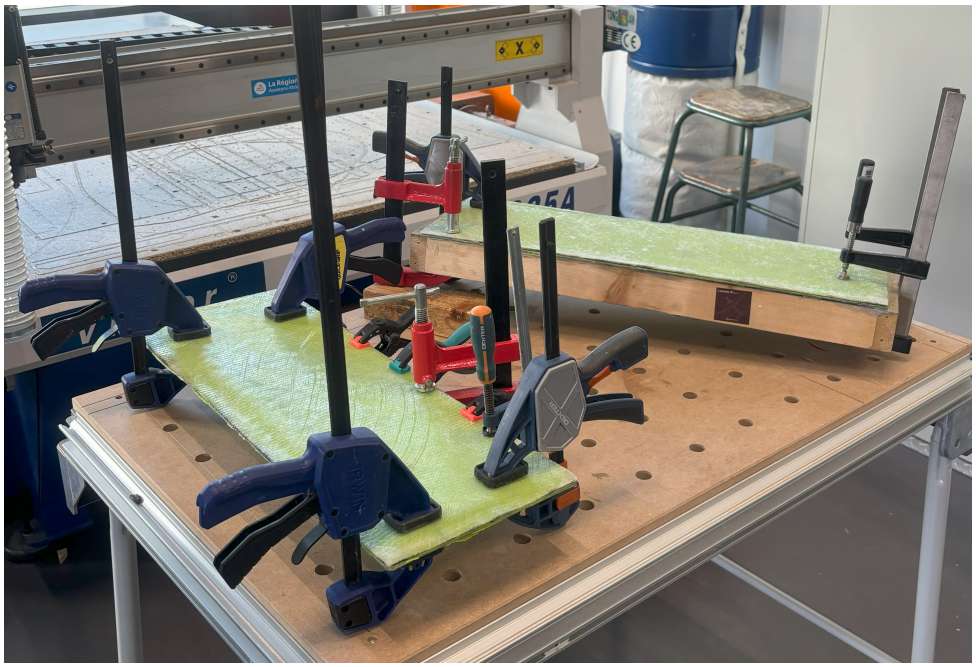

(a) Sealing stage of a composite wing in its mold

(b) Post-sealing root view of the MH-32 airfoil

Figure 27: Body assembly process and result

7.4 Oracover Skin Sections

The construction of the oracover-skinned wings and empennage closely followed the methods established during last year's build. Assembly began with the placement of the laser-cut ribs onto the bottom spar. Careful attention was paid to alignment and squareness before the top spar was added. Once these were secured, the doublers were installed at the root sections to increase local stiffness. With the primary spar structure in place, the aft shear web was added to the trailing edge of the ribs. For the V-tail, a 3mm balsa leading edge strip was applied which was soaked in water for easier bonding.

To ensure consistent assembly, 3D-printed PLA alignment tubes were embedded into the spar holes of both wing halves. These tubes not only helped align the panels during mounting but also reinforced the interface for repeated disassembly and transport.

The spar caps were constructed using flat layups of unidirectional carbon fiber on glass plates. Once cured, these strips were cut to size and glued onto the top and bottom of the main spars. For the outboard wings, which spanned a considerable length, an additional unidirectional carbon strip was bonded along the leading edge to increase stiffness and mitigate flex during flight.

The wing tips were glued directly onto the outboard wing panels using CA glue. These tips were previously 3D-printed and shaped to match the final airfoil profile.

Control surfaces, including ailerons and ruddervators, were laminated in fiberglass with strips of kevlar using a vacuum bagging process. The Kevlar was scored post-cure to act as a flexible hinge and was subsequently bonded to the body to finalize attachment.

Servo platforms were glued directly to the internal ribs using CA. The servos themselves were then fixed in place with hot glue for ease of access and quick servicing if needed.

To complete the construction, all external surfaces were covered in Oracover using a hot iron. The material was carefully tensioned and shrunk in place to achieve a tight, wrinkle-free finish that provided excellent aerodynamic performance.

7.5 Tail Body Section

The tail body construction began with the laser-cut wooden parts, which formed the internal structure of the fuselage joint. These included three bulkheads all cut from 5mm aviation plywood. The pieces were assembled on a flat jig to ensure alignment before being glued together using CA.

3D-printed components were iterated over, including the V-tail joint and the tail body diameter reducer. The reducer was particularly critical for transitioning between the tail boom and the empennage while housing the telemetry box. To ensure a clean finish and minimal drag, the printed reducer was carefully sanded and primed until the surface was smooth and free of print lines.

Once the V-tail joint was glued into place using epoxy paste, holes were drilled through the carbon tail boom tube to allow for mounting of the empennage assembly. Care was taken to ensure that the joint was aligned with the longitudinal axis before drilling.

Before final gluing, servo wires for the ruddervators were threaded through the carbon tube. To prevent rattling or interference with internal components, the wires were secured to the inside wall using small pieces of tape.

8 Aircraft Performance

To sum up, we present a compilation of the most important values used to assess the aircraft's performance. Analyzing our final model in Xflr5, we obtain:

Parameter	**Value**
ρ	1.18 kg/m^3
OEW	1.8 kg
MTOW	3.84 kg
$C_{L\max}$	1.08
C_D	0.0581 $+0.0360716(-0.09237 + C_L)^2$

Figure 28: Performance parameters

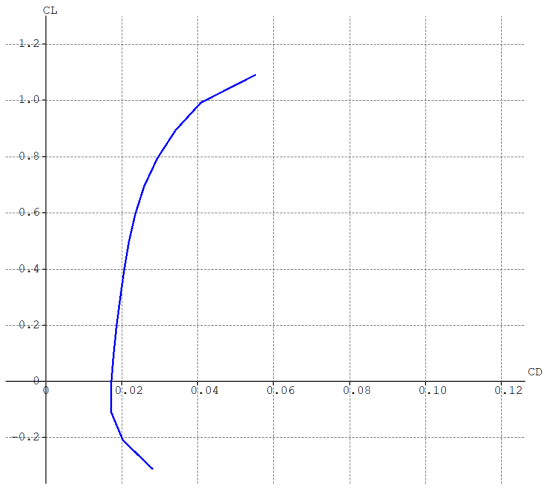

Figure 29: Aircraft Polar

We proceed to calculate the take-off velocity:

$$V_{TO} = 1.2 \times V_{\text{stall}} = 1.2 \times \sqrt{\frac{2W}{\rho S_w (0.8 C_{L\max})}} = 44.821 \text{ km/h}$$

With $W = m_T \times g$ with m_T total mass.
The take-off distance is given by the next equation:

$$x_{TO} = m_T \int_0^{V_{TO}} \frac{V}{T(V) - \frac{1}{2}\rho V^2 S_w (C_D - \mu_d C_L) - \mu_a m_T g} dV$$

To deduce the payload mass equation, we simply use the definition of MTOW:

$$MTOW = MPL + OEW \Rightarrow MPL = MTOW(\rho) - OEW$$

$$MPL = \frac{1}{g}\left(\frac{1}{2}\rho S_w V_{TO}^2 C_{L\max} - OEW\right)$$

$$\Rightarrow MPL = 3.46 \times \rho - 1.120$$

Using that last equation, we obtain the following figure:

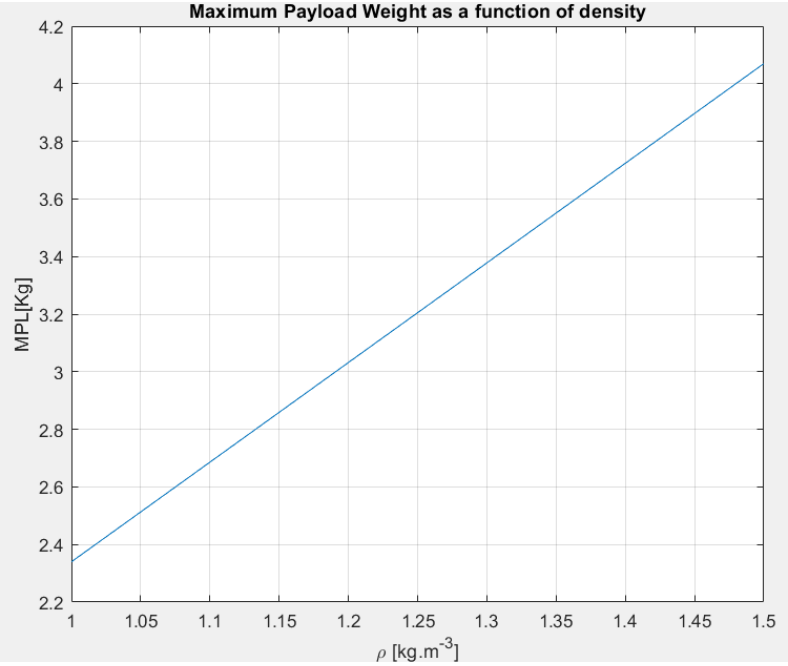

Figure 30: Payload Prediction as a function of air density

As for the trim, we can obtain the velocity and the flap deflection from the balancing equations:

$$L = \frac{1}{2}\rho S_w V^2 C_L \approx W$$

$$V_{\text{trim}} = \sqrt{\frac{2W}{\rho S_w C_{L\text{trim}}}} = 66.0389 \text{ km/h}$$

$$D = \frac{1}{2}\rho S_w (C_{D0} - K(C_{L\text{trim}} - C_{L\min,D})^2) V_{\text{trim}}^2 \approx T(\delta_{p,\text{trim}})$$

$$\delta_{p,\text{trim}} = \frac{1}{2}\rho S_w (C_{D0} - K(C_{L\text{trim}} - C_{L\min,D})^2) V_{\text{trim}}^2 a - b(V_{\text{trim}} - c)$$

9 Lessons Learned

The journey of developing the ECTanker with a new composite structure was filled with valuable lessons and practical challenges. Shifting from the previous wooden construction to composite materials involved new research and iterative experimentation. The theoretical knowledge from our courses was significantly enhanced through practical hands-on experience, especially in working with fiber layups and structural validation through experimental testing.

Our initial goal was to simplify manufacturing while ensuring reliability, leading us to adopt well-understood composite techniques rather than more advanced but riskier alternatives. Despite this cautious approach, composite manufacturing presented many complexities, particularly in managing vacuum pressure, achieving consistent laminate quality, and addressing structural interfaces.

In trying to keep costs down, we ended up going for cheaper materials and rushed making our molds. We opted for only one layer of tooling coat and 4 layers of reinforcement. Because of that, they weren't very strong and had many defects. Fixing these problems ended up taking a lot more time than we expected. Next time, more emphasis will be put on making a practice mold to start, ensuring we identify all possible missteps before creating our final molds.

A significant learning milestone came from producing our first composite body and stepping through all parts of fabrication to see when and how things can go wrong. Overall, many lessons were recorded over the semester which we hope will serve the future generations well.

10 Closure

The ECLift team is very proud of the results obtained during the months dedicated to the project. For most of the members, it has been a first-ever hands-on experience; very few students had previous expertise in the field of aircraft design or even aeronautics.

Through close collaboration, and a strong willingness to learn and create a great community of highly passionate students with a common goal, all the adversities were overcome. An example that with the right people, the sky is literally the limit.

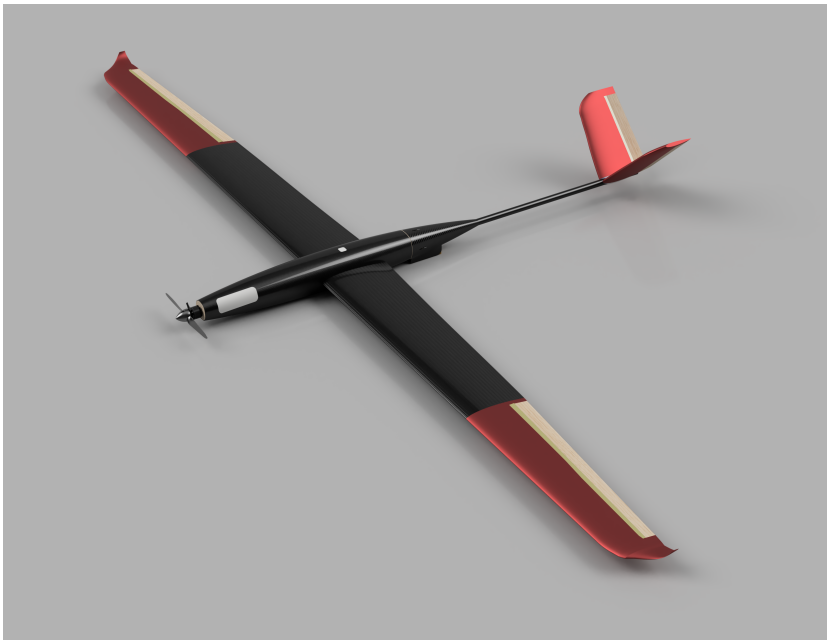

Figure 31: Rendered view of the competition aircraft showing the composite fuselage, carbon wings, and V-tail configuration.

We look forward to the XtraChallenge 2025, to learn from the best, and to share with the other participants more stories just like ours.

Annex I: Budget Breakdown

Avionics Budget

The avionics suite of the ECTanker includes a 6-channel receiver for pilot input, four digital metal gear servos for control surface actuation, and a SKYWALKER 50A ESC for power regulation and motor control. Power to the propulsion system was provided by a 3S 3200mAh LiPo battery, while a separate 2S 500mAh LiPo battery powered the flight control electronics through a UBEC.

To reduce costs and maintain modularity, wiring and connectors (XT60, XT90, bullet connectors) were kept simple and standardized across components. The propulsion system was centered around the EMAX GT2820/06 985KV brushless outrunner motor.

Component	**Unit Cost [€]**	**Quantity**	**Total Cost [€]**
6CH Receiver (FS-IA6)	8.62	1	8.62
EMAX ES3004 Servos	8.59	4	34.36
SKYWALKER 50A ESC	10.69	1	10.69
Main Battery (Generic 3200mAh 3S)	24.00	1	24.00
Aux Battery (2S 500mAh)	7.10	1	7.10
UBEC 4A	5.00	1	5.00
Connectors (XT60, XT90, Bullets)	3.00	1	3.00
Wiring (servo/power)	4.00	1	4.00
Emax GT2820/06 985KV Motor	28.00	1	28.00
APC 10x6 Propeller	2.00	1	2
Total			**126.77**

Table 10: Cost breakdown of the avionics system for the ECTanker.

Mold Manufacturing Budget

To estimate the cost of manufacturing the composite molds used in the ECTanker, we compiled the unit prices and quantities for the main materials involved. The molds for both the wings and the fuselage were produced using a top-bottom configuration, with each half reinforced using 4 layers of fiberglass. The total surface area of the molds was 0.58m^2 for the wings and 0.556m^2 for the fuselage, giving a combined area of 1.136m^2.

Each fiberglass layer covered the entire mold surface, resulting in:

$$A_{\text{total}} = 1.136\,\text{m}^2 \times 4\,\text{layers} \times 2\,\text{halves} = 9.09\,\text{m}^2$$

The fiberglass used had an areal density of $280\,\text{g/m}^2$, giving a total mass of:

$$m_{\text{glass}} = 9.09\,\text{m}^2 \times 280\,\frac{\text{g}}{\text{m}^2} = 2545.2\,\text{g} = 2.55\,\text{kg}$$

Assuming a 1:1 resin-to-fiber weight ratio:

$$m_{\text{epoxy}} = m_{\text{glass}} = 2.55\,\text{kg}$$

Material	**Unit**	**Unit Cost [€]**	**Quantity**	**Total Cost [€]**
Tooling Coat	kg	23.00	2.50	57.50
Epoxy	kg	17.65	2.55	44.01
Fiberglass	m^2	3.07	9.09	27.91
Total				**129.42**

Table 11: Cost breakdown for composite mold manufacturing.

Aircraft Bodies

Fuselage Body

The fuselage was built from two composite halves, each with both a top and bottom skin, giving a total surface area of $0.28\,\mathrm{m}^2$. Each side was laminated with one layer of $100\,\mathrm{g/m}^2$ fiberglass and one layer of $210\,\mathrm{g/m}^2$ carbon cloth. Additionally, three strips of unidirectional carbon (each 300 mm long and 15 mm wide) were placed per skin for local reinforcement, totaling six strips.

The internal structure included 4 ribs, 2 main and 2 aft shear webs, 4 formers, and a single stringer. All were laser-cut from aviation-grade plywood. To estimate their cost, we sum all relevant areas and related it to the sheet cost per area:

$$\mathrm{Cost}_{\mathrm{wood}} = A \cdot \frac{C_{\mathrm{sheet}}}{A_{\mathrm{sheet}}}$$

where $A = 14{,}841\,\mathrm{mm}^2$ is the total wood part area, and $C_{\mathrm{sheet}} = 11.90$ € is the cost of a 0.3 m * 0.6 m plywood sheet.

PLA was used for the landing baseplate, hatches, and water tank. These printed parts (6 g, 20 g, and 100 g respectively) were grouped under one combined cost. Additionally, 2.5€ was allocated for epoxy-glass bubble paste and curing consumables.

Material	**Unit**	**Unit Cost [€]**	**Quantity**	**Total Cost [€]**
Fiberglass	m^2	3.55	0.28	1.00
Carbon Fiber	m^2	21.60	0.28	6.05
Unidirectional carbon	m	0.70	1.80	1.26
Epoxy	kg	17.65	0.089	1.57
Plywood	m^2	252.32	0.0148	3.03
PLA	g	0.05	126	3.80
Epoxy-glass bubble paste	—	—	—	2.50
Vacuum bagging consumables	—	—	—	2.50
Total				**21.71**

Table 12: Fuselage body material budget

Inner Wing

Both inner wing sections were constructed using a composite sandwich skin, with each half receiving both top and bottom laminations. This brings the total skin area to $0.484\,\mathrm{m}^2$. One layer each of $100\,\mathrm{g/m}^2$ fiberglass and $210\,\mathrm{g/m}^2$ carbon cloth was applied to each side. For reinforcement, six strips of unidirectional carbon (530 mm long, 15 mm wide) were placed per side, totaling 12 strips across both halves of the inner wings.

Structural support was provided by plywood ribs and spars. The total surface area of these wood elements was $15{,}153\,\mathrm{mm}^2$. To join the wings to the fuselage, four 113 mm long carbon rods were used.

Material	Unit	Unit Cost [€]	Quantity	Total Cost [€]
Fiberglass	m^2	3.55	0.484	1.72
Carbon Fiber	m^2	21.60	0.484	10.46
Unidirectional Carbon	m	0.70	6.36	4.45
Epoxy	kg	17.65	0.154	2.72
Plywood	m^2	66.11	0.0152	3.04
Carbon rods	m	8.45	0.452	3.82
Epoxy-glass bubble paste	—	—	—	2.50
Vacuum bagging consumables	—	—	—	2.50
Total				**31.21**

Table 13: Inner wing material budget (for both wing sections)

Outer Wing

Each outer wing section included plywood ribs and spars, a balsa shear web doubler and aileron, and unidirectional carbon fiber tape used on both the leading edge and as spar caps. The ailerons were skinned in fiberglass and hinged with Kevlar strips. These components were duplicated for the left and right wing sections, and total quantities reflect this. PLA wing tips were 3D printed (20 g each), and carbon rods (4 pieces, each 121 mm) were used as spars.

Material	Unit	Unit Cost [€]	Quantity	Total Cost [€]
Plywood	m^2	252.32	0.0326	8.22
Balsa	m^2	250.00	0.0319	7.98
Unidirectional Carbon (leading edge)	m	0.70	1.23	0.86
Unidirectional Carbon (spar caps)	m	0.70	7.38	5.17
Fiberglass (ailerons)	m^2	3.55	0.0862	0.31
Kevlar strip	m	3.75	1.2	4.50
Carbon rods	m	8.45	0.484	4.09
PLA	g	0.05	40	2.00
Epoxy	kg	17.65	0.156	2.75
Total				**28.06**

Table 14: Outer wing material budget (both sections)

V-Tail

Each V-tail half was built using plywood ribs and spars, a balsa doubler, and a fiberglass-covered control surface. Two carbon tape strips (238 mm each) were used on the top and bottom spar caps. These reinforcement elements, together with a Kevlar hinge and a carbon rod, were duplicated for both sides. The total quantities reflect both V-tail halves.

The fiberglass (230 mm * 52 mm * 2 per half), Kevlar strip (230 mm * 32 mm * 2 per half), and epoxy were used to laminate and hinge the control surfaces.

Material	Unit	Unit Cost [€]	Quantity	Total Cost [€]
Plywood	m^2	252.32	0.0209	5.27
Balsa	m^2	250.00	0.0340	8.50
CF tape – spar caps	m	0.70	2.856	2.00
Fiberglass (ailerons)	m^2	3.55	0.0478	0.17
Kevlar strip	m	3.75	0.46	1.73
Carbon rod	m	8.45	0.470	3.97
PLA	g	0.05	40	2.00
Epoxy	kg	17.65	0.064	1.32
Total				**19.96**

Table 15: V-tail material budget (both sections)

Tail body

The tailbody structure consisted of plywood bulkheads, a central carbon tube for alignment and strength, and a collection of PLA parts used for internal mounts and mechanical interfaces. The total plywood area used was 12,726 mm^2.

The PLA components were grouped under a single entry totaling 60 g, while the main structural element—a 650 mm long carbon tube—was costed at 18.77 €/m.

Material	Unit	Unit Cost [€]	Quantity	Total Cost [€]
Plywood	m^2	252.32	0.0127	3.21
PLA	g	0.05	60	3.00
Carbon tube	m	18.77	0.650	12.27
Total				**18.48**

Table 16: Tailbody material budget

Summary of Costs

Subcomponent	Cost [€]
Fuselage	21.71
Inner Wing	31.21
Outer Wing (both sections)	28.06
V-Tail (both halves)	19.96
Tailbody	18.48
Landing Gear	20.00
Total Aircraft Body Cost	**139.42**

(a) Aircraft subcomponent material cost summary

Category	Cost [€]
Composite Molds	129.42
Electronics and Powertrain	126.77
Aircraft Body Materials	139.42
Total Program Cost	**395.61**

(b) Total aircraft cost summary for ECLift 2024–2025

Table 17: Overall budget breakdown

Annex II: Aircraft Drawings

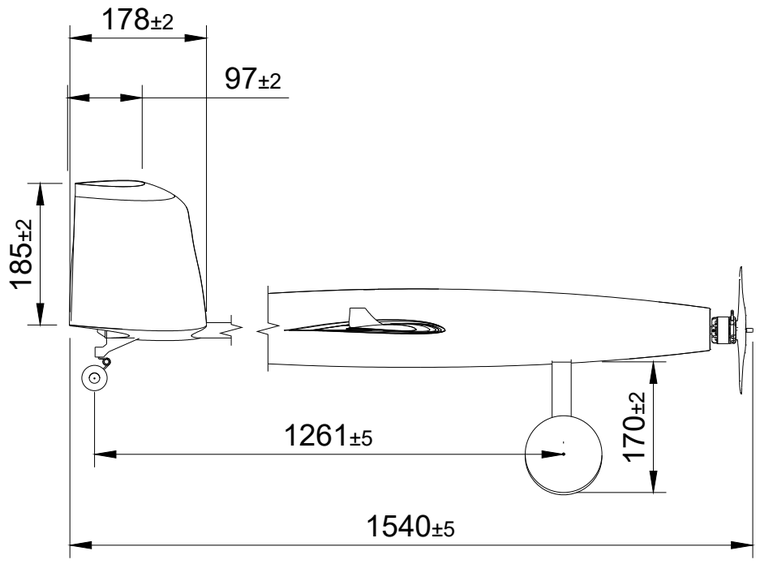

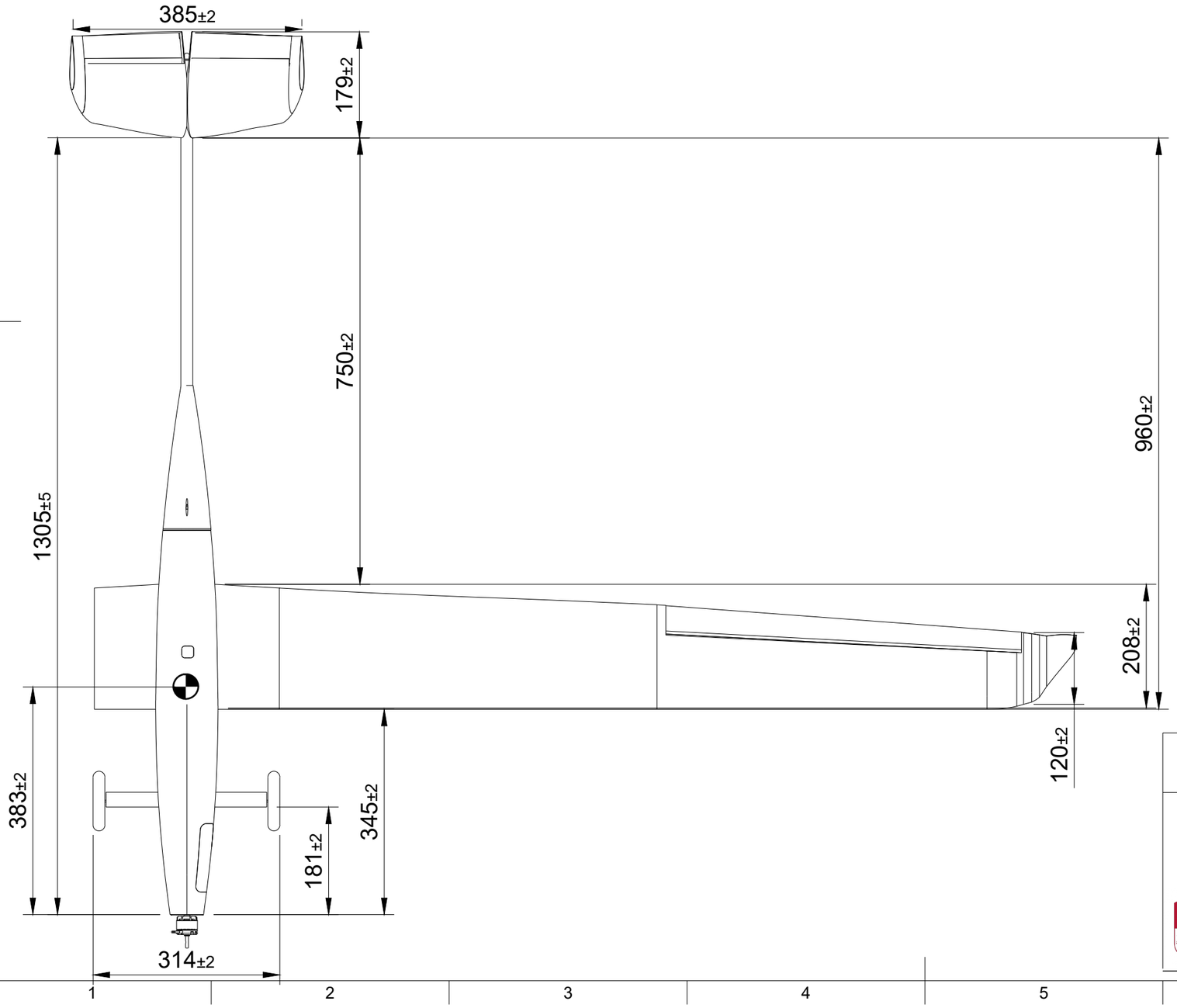

Relavent Parameters

Name	Value	Unit
Aircraft Length	1540	mm
OEW	1.8	kg
MTOW	3.8	kg
Cargo Capaciity	2	L
Wing Span	2990	mm
Wing Airfoil	MH32	-
M.A.C.	180	mm
Wing Area	0.48	m²
Wing Aspect Ratio	16.7	-
Empennage Area	0.08	m²
Empennage Airfoil	NACA 0012	-

Team 12 - ECLift	Title: Three View Drawing		Sheet: 1/4
	Date: 5/3/2025	Units: SI (mm,°)	Size: A3
	Department: Structures & Manufacturing		Scale: 1:6
	Xtra Challenge 2025		

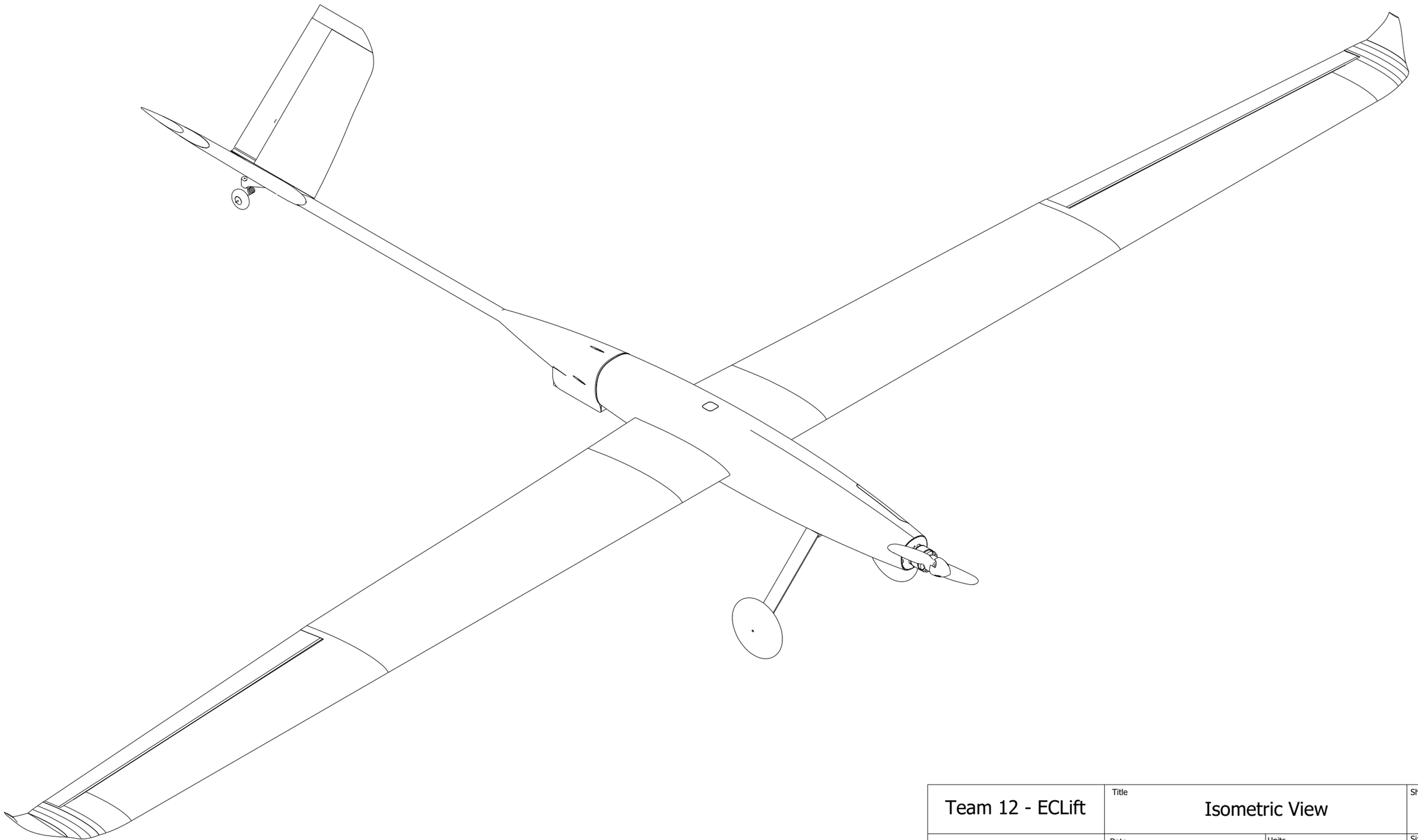

Team 12 - ECLift	Title: Isometric View		Sheet: 2/4
	Date: 5/3/2025	Units: SI (mm,°)	Size: A3
	Department: Structures & Manufacturing		Scale: 1:6
	Xtra Challenge 2025		

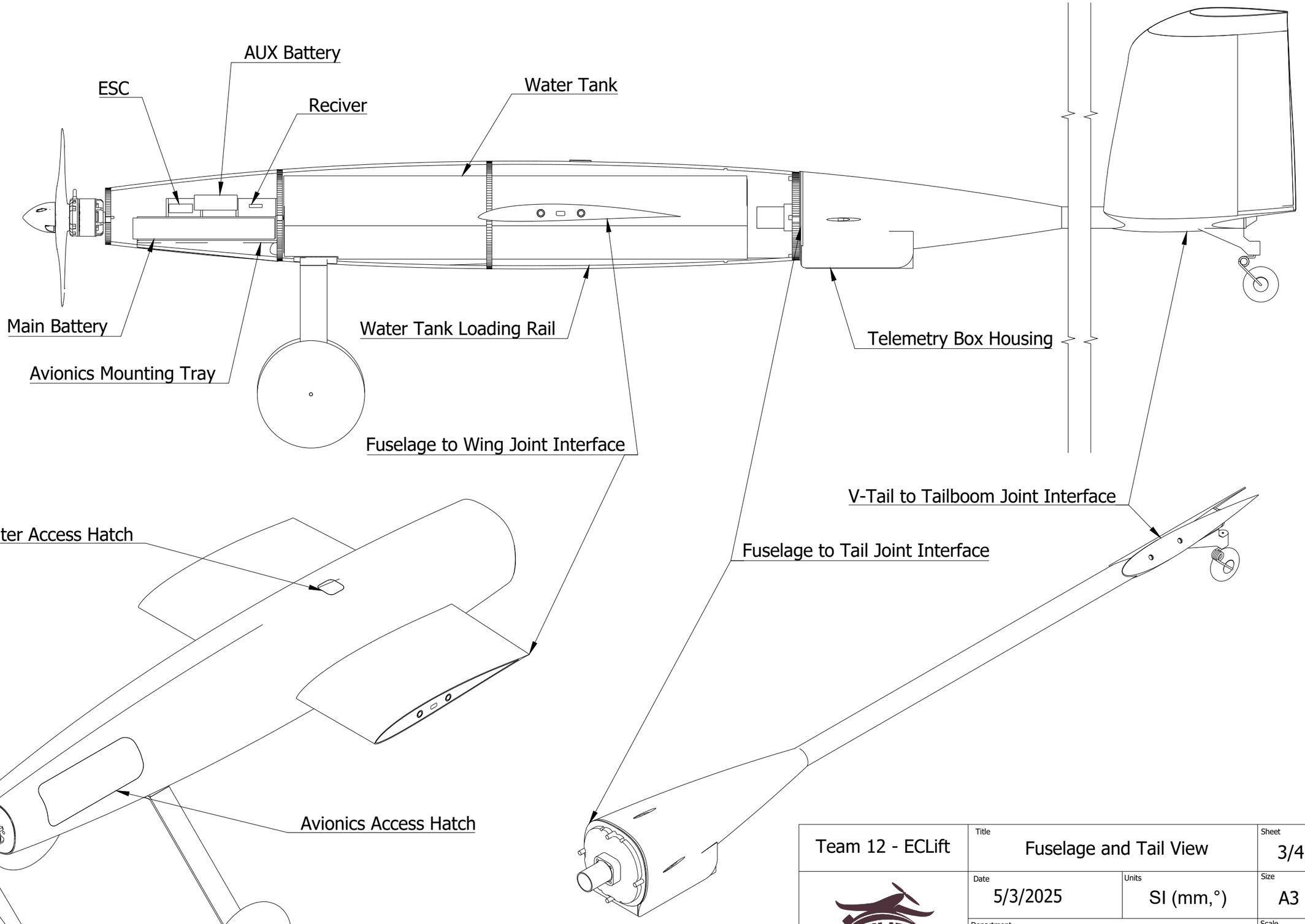

Team 12 - ECLift	Title: Fuselage and Tail View		Sheet: 3/4
	Date: 5/3/2025	Units: SI (mm,°)	Size: A3
	Department: Structures & Manufacturing		Scale: 1:5
	Xtra Challenge 2025		

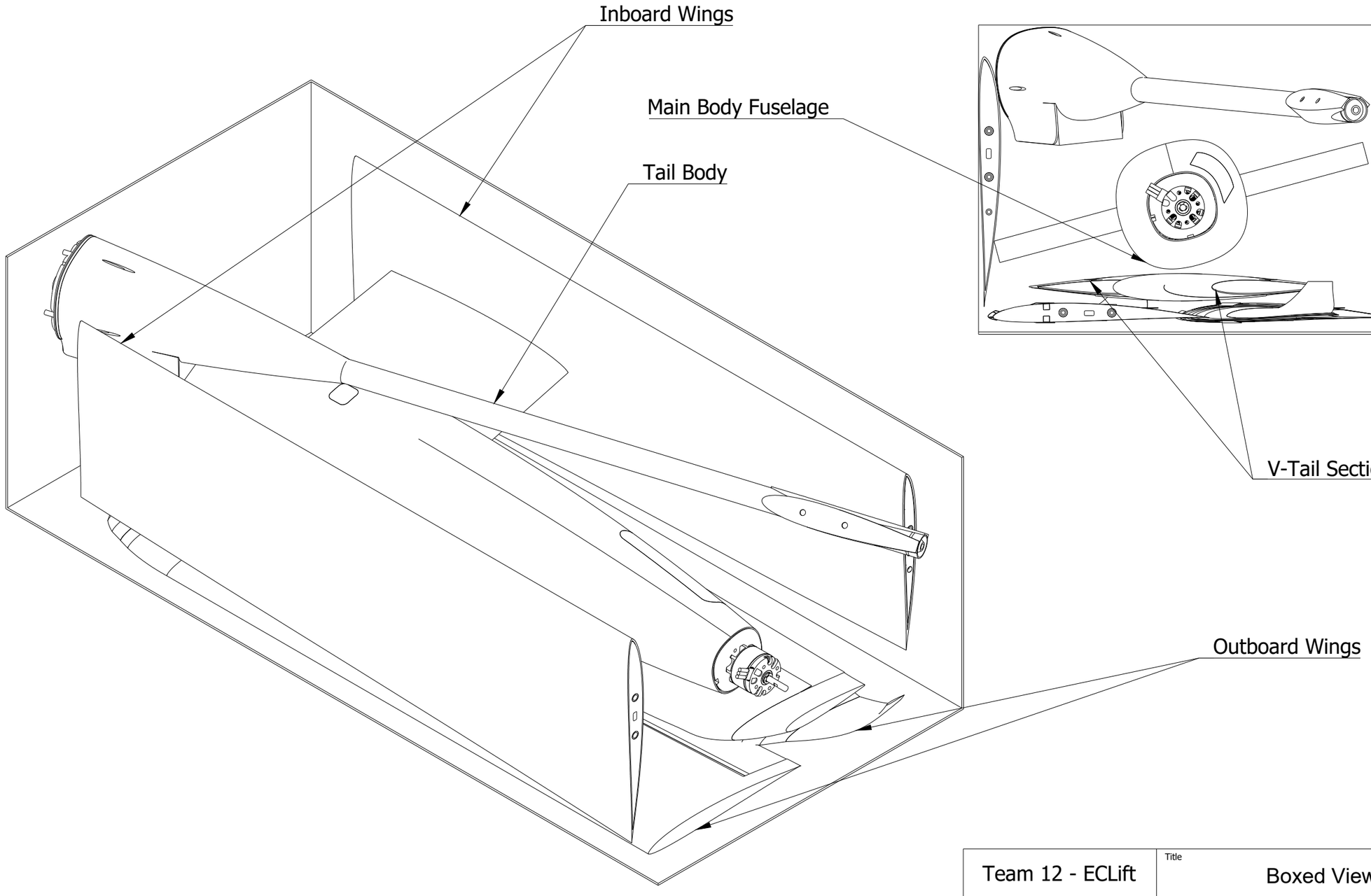

Team 12 - ECLift	Title: Boxed View		Sheet: 4/4
	Date: 5/3/2025	Units: SI (mm,°)	Size: A3
	Department: Structures & Manufacturing		Scale: 1:3.5
	Xtra Challenge 2025		